A new clustering method for the diagnosis of CoVID19 using medical images

Himanshu Mittal[1] · Avinash Chandra Pandey[1] · Raju Pal[1] · Ashish Tripathi[2]

Abstract

With the spread of COVID-19, there is an urgent need for a fast and reliable diagnostic aid. For the same, literature has witnessed that medical imaging plays a vital role, and tools using supervised methods have promising results. However, the limited size of medical images for diagnosis of CoVID19 may impact the generalization of such supervised methods. To alleviate this, a new clustering method is presented. In this method, a novel variant of a gravitational search algorithm is employed for obtaining optimal clusters. To validate the performance of the proposed variant, a comparative analysis among recent metaheuristic algorithms is conducted. The experimental study includes two sets of benchmark functions, namely standard functions and CEC2013 functions, belonging to different categories such as unimodal, multimodal, and unconstrained optimization functions. The performance comparison is evaluated and statistically validated in terms of mean fitness value, Friedman test, and box-plot. Further, the presented clustering method tested against three different types of publicly available CoVID19 medical images, namely X-ray, CT scan, and Ultrasound images. Experiments demonstrate that the proposed method is comparatively outperforming in terms of accuracy, precision, sensitivity, specificity, and F1-score.

Keywords CoVID19 diagnosis · Clustering · Metaheuristic algorithm · Gravitational search algorithm

1 Introduction

With the rapid outbreak of the Corona virus Disease (CoVID19) around the globe [1], the World health organization (WHO) has been declared CoVID19 as a Public Health Emergency of International Concern (PHEIC) [2]. Pathogenically, the virus identified in CoVID19 is "severe acute respiratory syndrome coronavirus 2" (SARS-CoV-2) which is quite distinct from other respiratory viruses like MERS-CoV, SARS-CoV, avian influenza, and influenza [3]. Usual symptoms in a COVID19 patient are fever, dry cough, and tiredness. Other signs experienced by patients include sore throat, diarrhea, headache, loss of taste or smell, and rash on the skin and severely infected patients have symptoms of breathing difficulty, chest pain, and Multi-Organ Failure (MOF) [4]. Despite worldwide efforts to control the growth of CoVID19, the number of CoVID19 incidences is still rising at a reproduction rate of 3.77 [5]. Globally, there are over 6.15 million confirmed cases, out of which more than 2.63 million patients have recovered while 371,700 patients died, as of the date (1 June 2020) [6]. Moreover, USA with more than 1.8 million confirmed cases is the most severely affected country, followed by Brazil, Russia, United Kingdom, Spain, and Italy, with more than 200 thousand confirmed cases to date. India, being the second-largest population country, has also a significant rise in the number of CoVID19 cases. At the time of this writing article, there are nearly around 200 thousand confirmed cases in India with a death count of 5,394. Presently, there are no approved antiviral drugs or treatment regimens to cure COVID19 [4].

Meanwhile, real-time polymerase chain reaction (RT-PCR) can be conducted to confirm the diagnosis of CoVID19 [7]. However, it has been observed that this method has several limitations, such as time-consuming, low true-positive rates, and high false-negative rates [7, 8]. Due to the high communicable behavior of CoVID19, such limitations raises a major concern in the current

✉ Avinash Chandra Pandey
  avish.nsit@gmail.com

  Himanshu Mittal
  himanshu.mittal224@gmail.com

[1] Jaypee Institute of Information Technology, Noida, India

[2] Malaviya National Institute of Technology, Jaipur, India

Fig. 1 Representative sample images of non-CoVID19 patients: **a** chest Xray, **b** chest CT-scan, and **c** lung Ultrasound
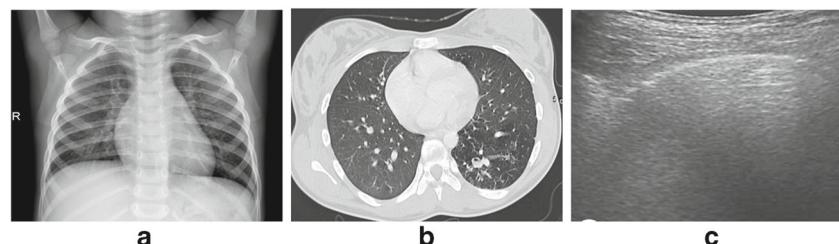
epidemic situation. If an infected person is not diagnosed and treated timely, then the infected person may act as a carrier of the virus and spread it among healthy people unknowingly. Therefore, early identification of the infected people would help to quarantine them, which would be advantageous in declining the growth of CoVID19. As an alternative, clinical observations [9] have observed high sensitivity in diagnosing the CoVID19 through medical imaging modalities. There are irregular ground-glass opacities in chest images of the infected people [10]. Figures 1 and 2 illustrate representative samples of three medical imaging modalities, i.e. chest X-ray, chest CT-scan, and lung ultrasound images, of non-CoVID19 and CoVID19 patients, respectively. In general, the manual analysis of such images requires expert radiologists which makes this costly and error-prone process. To alleviate the same, computer-aided methods could facilitate as diagnostic aids for CoVID19. Fang et al. [11] has observed that the diagnosis of CoVID19 through imaging patterns in the chest images is much accurate than RT-PCR. Similar observations are also reported by Xie et al. [12]. Recently, many supervised learning methods have been proposed in which the concept of transfer learning is mainly applied in which a pre-trained deep learning model is used as a feature extractor. Deep learning models are not employed directly due to the unavailability of a large dataset of labeled chest images for CoVID19. Therefore, researchers have extracted deep features through transfer learning, and then, classification is performed through supervised models like decision tree, AdaBoost, support vector machine, and many more [4, 13].

Literature has witnessed that the accuracy attained by supervised learning on deep features, i.e. features extracted

through transfer learning, is around 90%. However, the availability of limited medical images of CoVID19 may result in overfitting and thus impact the generalization ability of these learnable models. Moreover, the key requirement of supervised learning is labelled data [14, 15]. In such scenarios, literature has witnessed that unsupervised learning is quite efficient in determining patterns within the unlabelled data, especially clustering [16, 17]. Clustering methods induce inferences by discovering constitutional structures from the unlabelled dataset [18]. Therefore, the motivation of this paper is employing unsupervised learning on deep features for the diagnosis of CoVID19 from the medical chest images.

In literature, one of the most popular unsupervised methods is Kmeans. Kmeans method clusters the unlabelled dataset into distinct unified clusters according to certain similarity measure [19]. Sometimes, Kmeans method suffers from a number of demerits like, biased towards initial clusters, converges pre-maturely, and produces local optima [20]. To mitigate such limitations, metaheuristic methods have been successful for clustering [21, 22]. Metaheuristic methods are mathematical models that mimic the unique optimization behavior of the natural systems [23]. Generally, metaheuristic methods have exhibited good performance on numerous nonlinear and complex optimization problems [24–26]. From the last two decades, they have been an integral part of many real-world applications ranging from design to business planning [27, 28]. Some popular metaheuristic methods are genetic algorithm [29], differential algorithm [30], particle swarm optimization [31], ant colony optimization [32], biogeography-based optimizer [33], and artificial bee colony [34]. There are many other phenomena in nature
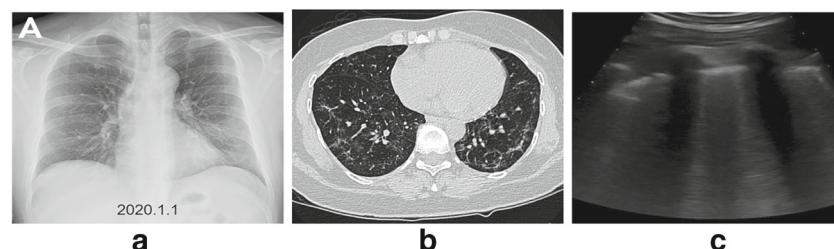

Fig. 2 Representative sample images of CoVID19 patients: **a** chest Xray, shows opacities in the left lower and right upper lobes, **b** chest CT-scan, shows multifocal bilateral ground-glass opacities., and **c** lung Ultrasound, showing small sub-pleural consolidation and pleural irregularities

that have been utilized for solving other types of real-world problems [35]. One such common phenomenon is Newton's law of gravity and motion which inspired Rashedi et al. [36] to introduce a new metaheuristic method termed as gravitational search algorithm (GSA). Gravitational search algorithm (GSA) has achieved effective results on many optimization problems like image segmentation, energy conservation, parameter selection, and clustering. A comprehensive survey of different applications of GSA is reviewed in [37]. The prominent attribute of GSA is the gravitational interaction among the considered solutions which makes it a unique and stable method [38]. Moreover, it updates solutions based on the fitness of each solution and distance among them, [39]. Further, it considers current solutions to achieve an optimal solution and requires only a single predefined parameter i.e., gravitational constant. [40]. Therefore, this paper leverages the strengthens of GSA for the optimal clustering of image features.

GSA [36] is inspired by the Newtonian law of gravity and motion. It considers a swarm of solutions as objects which update the solution collectively. In GSA, every object interacts with other objects under the gravitational force. Initially, GSA explores the search space by allowing a high number of objects for interaction. The number of objects is linearly decreased to perform exploitation which is controlled by *Kbest* function [41]. In GSA, the fitness of an object determines its mass, and thus, a heavier object represents a better solution. Therefore, the position of the heaviest object corresponds to the optimal solution of the considered problem. Though GSA is quite efficient, there are still chances of improvement in the solution precision. Therefore, this paper presents a novel variant of GSA, improved GSA (IGSA), to enhance the vicinity to optimal solutions. Further, the proposed variant is employed to obtain optimal clusters in the proposed clustering method for the CoVID19 diagnosis.

The overall contribution of this paper is four folds:

- A novel variant of the gravitational search algorithm, improved gravitational search algorithm (IGSA), is presented,
- A new clustering method, Kmeans-based improved gravitational search algorithm clustering (KIGSA-C) method, has been introduced for the diagnosis of CoVID19,
- An extensive experimental analysis of IGSA has been conducted against 16 metaheuristic algorithms over 17 standard benchmark functions belonging to unimodal and multimodal categories. Further, the real-parameter single-objective optimization problems from IEEE Congress on Evolutionary Computation (CEC) 2013 are considered to validate the performance of the proposed variant on translated and shifted benchmark

functions. The results are studied over four different dimensional settings, i.e. 10, 30, 50, and 90, and
- The proposed KIGSA-C method is experimentally evaluated against two methods, namely Kmeans and Kmeans-based gravitational search algorithm clustering (KGSA-C). For experimental analysis, three types of medical chest images, i.e. X-ray, CT-scan, and Ultrasound images, of non-CoVID19 and CoVID19 patients are taken from the publicly available links. The effectiveness of the considered methods is compared in terms of confusion matrix along with five classification measures, namely sensitivity, specificity, precision, F1-score, and accuracy [42].

The organization of the paper is as follows; Section 2 discusses the related work. The feature extraction through transfer learning along with GSA is detailed in Section 3. Section 4 discusses the proposed method along with new variants of GSA followed with the experimental results in Section 5. Lastly, the conclusion is drawn in Section 6.

2 Related work

Xu et al. [43] used a convolutional neural network (CNN) for transfer learning on the CT images and performed classification between influenza-A viral and CoVID19 pneumonia with an accuracy of 86.7%. On the same lines, Wang et al. [44] used a modified inception model instead of CNN to obtain 89.5% accuracy. Further, Hemdan et al. [45] performed a comparative study of various deep learning models on the chest X-ray images and reported the best accuracy of 90.00%. However, Sethy et al. [46] extracted deep features from the X-ray images and then trained the support vector machine to classify between positive and negative cases. The proposed model achieved an accuracy of 95.38%. Further, Wang and Wong [47] modeled a deep learning framework, COVID-Net, for multi-class classification of chest X-ray images among normal, bacterial infection, viral infection, and CoVID19 infection. This study achieved an accuracy of 83.5%. For similar classes, Farooq and Hafeez [48] utilized a pre-trained ResNet-50 architecture and reported an accuracy of 96.23%. Further, Maghdid et al. [49] employed supervised methods on features obtained through AlexNet and obtained an accuracy of 94.00%. In literature, GSA has been modified or hybridized with different characteristics to improve its performance on various types of non-linear, non-differentiable, and large search space problems. Shaw et al. [50] used the concept of opposition-based learning to propose opposition-based GSA (OGSA), which achieved better solution precision. Chatterjee et al. [51] applied the wavelet theory in GSA and presented enhanced GSA

(EGSA(I)) to improve the exploration ability. In [52], Mirjalili et al. introduced enhanced GSA (EGSA(II)) in which the velocity parameter incorporates the exploitation feature of PSO. Sarafrazi et al. [53] introduced enhanced GSA (EGSA(III)), which modified the position parameter with disruption operator. Moreover, a modified GSA was proposed by Niknam et al. [54] by incorporating a self-adaptive mutation method in GSA. Li et al. [55] introduced chaotic behavior in the position equation and presented a chaotic gravitational search algorithm (CGSA). Mirjalili et al. [56] proposed adaptive gbest GSA (GGSA) to improve the exploitation at later iterations. Further, Khajehzadeh et al. [57] employed an adaptive maximum velocity constraint in the modified gravitational search algorithm (MGSA(I)). The modified gravitational search algorithm (MGSA(II)) [58] uses the chaotic operator to prevent premature convergence. In piecewise-GSA (PGSA), Li et al. [59] modified the gravitational constant with piecewise equation. Similarly, Li et al. [60] proposed a weighted inertia mass for each object to accelerate convergence. To reduce the centre bias behavior of GSA, Davarynejad et al. [61] introduced a mass-dispersed gravitational search algorithm (mDGSA). Moreover, a chaotic $Kbest$ gravitational search algorithm (CKGSA) [62] introduces chaotic behavior based on logistic mapping in $Kbest$ function. It makes GSA escape the local optima as chaos behavior has shown better-searching behavior than stochastic [58, 63]. However, chaotic behavior is dependent on initial conditions which make this biased towards the initial settings. Mittal et al. [64] proposed logarithmic $Kbest$ GSA (LKGSA) in which $Kbest$ function decreases logarithmically which results in allowing heavier objects to exert force for more number of iterations. However, LKGSA performs exploration for a few iterations only. It diminishes the ability of the LKGSA to explore the search space exhaustively. Further, exponential $Kbest$ GSA (EKGSA) [65] defines the exponentially decrease in $Kbest$ which allows $Kbest$ function to perform exploration at an early stage and exhaustive exploitation at the later stage. Although EKGSA shows exhaustive exploitation at later iterations, the convergence precision still lacks.

3 Preliminaries

3.1 Transfer learning as feature extraction

The availability of limited labeled data for a problem domain always leads the training of a deep learning model towards overfitting, especially when the number of samples in the data is much smaller in comparison to the data dimensionality [4]. Moreover, it has been witnessed in the literature that the performance of the raw deep learning model is not significant on CoVID19 images even if strategies like fine-tuning [66] and data augmentation [67], are applied to reduce the problem of limited or imbalanced data. To resolve this, the concept of transfer learning, termed as transfer learning as feature extractor (TLFE), is employed in which a pre-trained deep learning model learned on a cross-domain dataset is used as a feature extractor for the current dataset [4]. The extracted features are low in dimension, which is further utilized with other learning models to perform the classification. This strategy of transfer learning advantages the learning processing in many ways, such as overcoming overfitting, reducing computational time, and decreasing required resources [13]. Generally, there are two types of deep learning models, namely the convolutional neural network (CNN) and recurrent neural network (RNN). RNN models are better in understanding the textual data while CNN models are efficient in encoding the visual patterns from images [68]. Therefore, a pre-trained CNN model is utilized to extract the feature vectors from the image dataset.

3.1.1 Convolutional Neural Network (CNN)

In a CNN [69], there are generally four kinds of layers, namely convolutional layer, non-linear activation layer, pooling layer, and fully-connected layer. Different combinations of these layers present different CNN models. Along with these layers, different CNN models use different classification layers, like sigmoid or softmax, to perform the classification task. Figure 3 depicts the architecture of AlexNet model for image classification. There are many

Fig. 3 A typical convolutional neural network (CNN) [71]

Input data   Conv1   Conv2   Conv3   Conv4   Conv5   FC6 FC7 FC8

$227 \times 227 \times 3$ $55 \times 55 \times 96$ $27 \times 27 \times 256$ $13 \times 13 \times 384$ $13 \times 13 \times 384$ $13 \times 13 \times 256$ 4096   4096
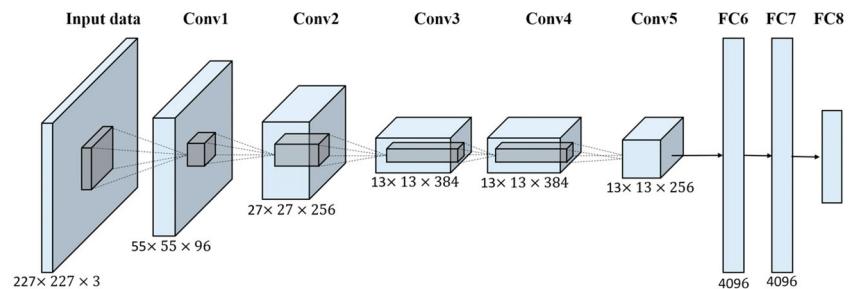
pre-trained CNN models publicly available for TLFE like AlexNet, VGG, ResNet, Inception, and MobileNet. [70]. In general, the convolutional layer performs the convolution operation of filtering the image features by applying 'K' kernels. The output generated from this layer is termed as feature maps. The non-linear activation layer brings non-linearity in the system by applying non-linear, continuous, and differential functions such as sigmoid, tanh, and rectified linear unit (ReLU). Generally, CNN prefers ReLU for a non-linear activation layer whose mathematically formulation is defined in (1).

$$f(x) = \max(x, 0) \tag{1}$$

where, $f(x)$ corresponds to the output ReLU function for the input value x. It can be observed that ReLU returns 0 if x is less than 0, else it attains x only. Figure 4 illustrates the same functioning of ReLU.

Further, the pooling layer is applied in CNN to perform down-sampling and fetch important structural features through either max-pooling or average-pooling. Max-pooling computes the maximum value in the considered region of an image while average-pooling calculates the average value over the studied region. Usually, a filter of size 2×2 is moved around the image to perform down-sampling. Moreover, it has been observed in the literature that the max-pooling layer is more efficient than the average-pooling layer in CNN models comparatively. Lastly, the fully-connected layer, alias dense layer, corresponds to the layer in which each node receives input from each node of the previous layer. To apply this layer in CNN, a flattening operation is performed first, which transforms visual features into feature vectors which are generated from the combination of convolutional, non-linear activation, and pooling layer. After that, CNN employs a set of fully-connected layers till the last layer, i.e. classification layer. The classification layer evaluates the probability and maps the computed feature vectors to class labels. If the classification problem is binary, then the sigmoid function is usually applied in the last layer, else softmax function is used for multi-class problems. To perform the feature extraction, the last layer of a pre-trained CNN model is truncated and the remaining combination of layers, i.e. convolutional, non-linear activation, pooling, and fully-connected, are used to extract the feature vector.
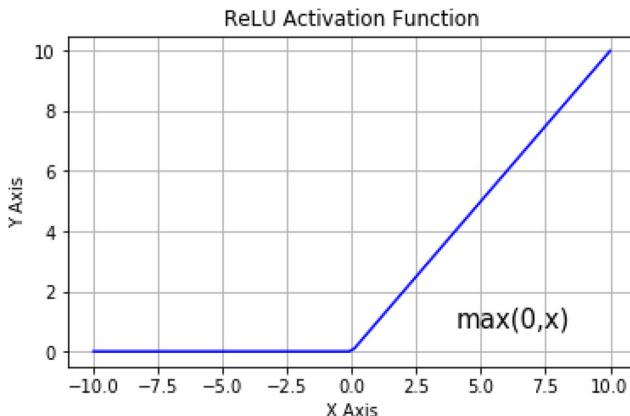
3.2 Gravitational Search Algorithm (GSA)

In GSA, a swarm of solutions is considered to update the solutions collectively. It assumes every solution as an object and allows them to interact with each other under the gravitational force. Initially, GSA explores the search space by allowing a high number of objects for interaction and linearly decreases the number of objects to perform exploitation. Specifically, the search strategy is controlled by the $Kbest$ function. The larger value of this function represents exploration, while its lower value corresponds to the exploitation of GSA. Moreover, the fitness of an object determines its mass, and thus, a heavier object means a better solution with better fitness. Hence, GSA converges every object towards the heaviest one based on the laws of gravity and motion. Moreover, the position of the heaviest object corresponds to the optimal solution of the considered problem.

Assume there are P objects in a d dimensional space, each object (X_i) can be represented as (2).

$$X_i = (x_i^1, ..., x_i^r, ..., x_i^d), i = 1, 2, ..., P \tag{2}$$

where, $x_i{}^r$ corresponds to the position of ith object in the rth dimension. The position of the ith object at t^{th} iteration is updated according to the (3).

$$x_i^r(t+1) = x_i^r(t) + v_i^r(t+1). \tag{3}$$

In (3), $v_i^r(t+1)$ corresponds to the updated velocity of ith object at t^{th} iteration and computed by (4).

$$v_i^r(t+1) = rand_i \times v_i^r(t) + a_i^r(t), \tag{4}$$

According to the law of motion, the acceleration ($a_i^r(t)$) of each object is computed which is formulated in (5) for i^{th} object at t^{th} iteration.

$$a_i^r(t) = \frac{F_i^r(t)}{M_i(t)}, \tag{5}$$

here, $F_i^r(t)$ and $M_i(t)$ correspond to the total force and mass of ith object at t^{th} iteration respectively.

GSA assumes gravitational mass and inertia mass of an object equal. Therefore, M_i is calculated in every iteration t by (6) for i^{th} object with fitness value ($fit_i(t)$)

Fig. 4 Rectified Linear Unit (ReLU) [72]

where $best(t)$ and $worst(t)$ are measure by (8) and (9) respectively for minimization problem.

$$M_i(t) = \frac{m_i(t)}{\sum_{j=1}^{P} m_j(t)}, \tag{6}$$

$$m_i(t) = \frac{fit_i(t) - worst(t)}{best(t) - worst(t)}, \tag{7}$$

$$best(t) = \min_{j \in \{1,...,P\}} fit_j(t) \tag{8}$$

$$worst(t) = \max_{j \in \{1,...,P\}} fit_j(t) \tag{9}$$

Moreover, the total force $F_i^r(t)$ is defined as a randomly weighted sum of the force by other $Kbest$ objects in r^{th} dimension and is defined as (10).

$$F_i^r(t) = \sum_{j=1, j \neq i}^{Kbest} rand_j F_{ij}^r(t), \tag{10}$$

where, $rand_j \in [0, 1]$ is a random number. F_{ij} is the force of jth object on i^{th} object and is computed by (11).

$$F_{ij}^r(t) = G(t) \frac{M_i(t) \times M_j(t)}{R_{ij}(t) + \epsilon}(x_j^r(t) - x_i^r(t)) \tag{11}$$

In (10), $Kbest$ is computed as (12) at t^{th} iteration.

$$Kbest(t) = final\_per + \left(\frac{1-t}{\max\_it}\right) \times (100 - final\_per), \tag{12}$$

where max_it is the maximum number of iterations and $final\_per$ is the percentage of objects which apply force to others. Equation (12) shows that the value of $Kbest$ decreases linearly over iterations. To illustrate the trend of the $Kbest$ function, Fig. 5 depicts the number of iterations along the x-axis and values attained by this function along the y-axis. It is observable from the figure that the $Kbest$ function decreases linearly. At the end of the stopping criteria, the position of the heaviest object among the $Kbest$ objects defines the optimal solution. The pseudo-code of GSA is presented in Algorithm 1 [73].
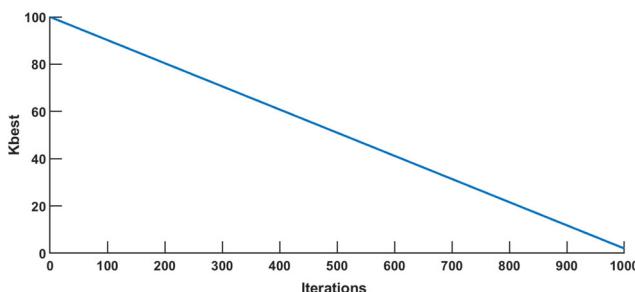
Fig. 5 $Kbest$ over iterations

Algorithm 1 Gravitational Search Algorithm (GSA) [73].

Input: Let P be the number of objects in d-dimensional space. Assume initial value of gravitational constant (G_0).
Output: Position of heaviest object corresponds to optimal solution.
1: Randomly initialize the population;
2: **while** termination condition does not meet **do**
3:    Compute the fitness (fit), G, and mass (M);
4:    Compute $Kbest$ as:
5:    $Kbest(t) = P \times \frac{final\_per + (1 - \frac{t}{max\_it}) \times (100 - final\_per)}{100}$,
6:    Compute acceleration (a);
7:    Update the velocity (v);
8:    Update the position (x) as:
9:    $x(t+1) = x(t) + v(t+1)$
10: **end while**

---

4 Proposed method

This paper presents a new clustering method, Kmeans-based improved gravitational search algorithm clustering (KIGSA-C) method, for the diagnosis of CoVID19 from medical chest images i.e., X-ray, CT-scan, and Ultrasound images. Figure 6 presents the architecture of the proposed method. First, the publicly available medical images of the infected and non-infected persons are collected. Then, the visual quality of all the collected images is improved through pre-processing. Here, standard normalization techniques of image processing are applied. Next, the feature extraction phase is performed in which a pre-trained CNN model acts as TLFE and aids in extracting prominent deep features for each input image.

Since the initial population of a metaheuristic algorithm is initialized randomly, this may impact the algorithm convergence as well as may lead it to local optima. Therefore, the extracted features are optimally clustered through Kmeans-based improved gravitational search algorithm (KIGSA). In KIGSA, the solutions obtained from Kmeans are used for the population initialization of the proposed variant, improved gravitational search algorithm (IGSA). Further, the proposed IGSA updates the solutions to obtain optimal cluster centroids. The objective function considered by IGSA to obtain the optimal solution is the sum of squared Euclidean distance between the features and corresponding cluster centroid. Further, (13) equates the mathematical formulation for the considered objective function.

$$Argmin_{\{C_1,\cdots,C_i,\cdots,C_n\}} : \sum_{i=1}^{n} \sum_{j=1}^{N} \left(C_i - x_j\right)^2 \tag{13}$$

where, C_i and x_j correspond to the ith cluster centroid and j^{th} feature vector, respectively. Moreover, N represents the
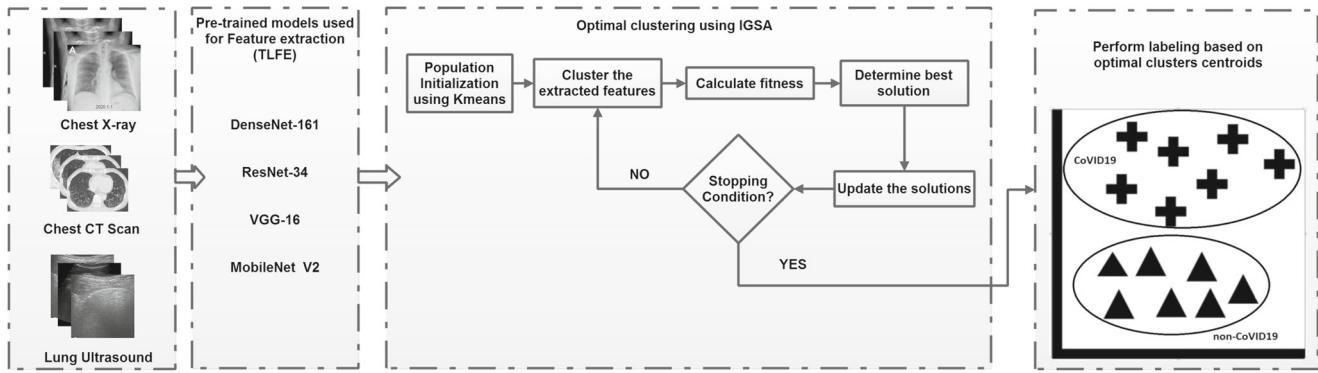
Fig. 6 The workflow of the proposed method

number of feature vectors, while *n* depicts the number of clusters to be formed. As the diagnosis of CoVID19 is a binary classification problem, the number of formed clusters is two. Finally, the obtained optimal cluster centroids are used to perform the mapping of input image features with labels. Further, the pseudo-code of the proposed method is described in Algorithm 2. The proposed variant, improved gravitational search algorithm (IGSA), is detailed in the following section.

Algorithm 2 Proposed KIGSA-C method.

Input: Let X be the set of medical images.
Output: Predicted classes for each image in X.
1: Perform TLFE on X to obtain feature vectors;
2: **for** each individual of KIGSA **do**
3:     Generate K cluster centroids through Kmeans;
4:     Compute the fitness (fit) using the considered objective function;
5: **end for**
6: **while** termination condition does not meet **do**
7:     Update each individual according to proposed IGSA;
8:     Compute the fitness (fit) using the considered objective function;
9: **end while**
10: Identify the global best as optimal cluster centroid;
11: Use the optimal cluster centroid to cluster the feature vectors;
12: Predict the label for each feature vector.

4.1 Proposed improved GSA (IGSA)

In GSA, the $Kbest$ function regulates the trade-off between exploration and exploitation. This function determines the 'K' number of best solutions which apply the gravitational force in an iteration and its value decreases linearly with increasing iterations. Hence, the transition from exploration to exploitation in GSA is linear [74]. Moreover, in later iterations, the small value of $Kbest$ results in reduced exploration ability [75]. Henceforth, the probability of GSA to trap into local optimum increases [76] which results in lacking the ability to achieve better solution precision.

To alleviate the same, a novel variant of GSA, improved gravitational search algorithm (IGSA), is proposed in which the $Kbest$ function is modified. Equation 14 formulates the mathematical definition of the new $Kbest$ function at t^{th} iteration.

$$Kbest(t) = P - \left(P \times \left(\left(\frac{t}{max\_it} \right)^{(1/final\_per)} \right) \right) \quad (14)$$

where, P, max_it and $final\_per$ correspond to population size, maximum iterations, and minimum percentage of objects, respectively. Further, Fig. 7 illustrates different values attained by the modified $Kbest$ over 1000 iterations for P as 50.

It can be observed from Fig. 7 that modified $Kbest$ does not decrease linearly. Moreover, it starts favouring exploitation over exploration after a few iterations. It results in achieving better solution precision as heavier objects exploit the search space over more iterations comparatively.

4.2 Time complexity of KIGSA-C method

The time complexity of the proposed method to perform clustering is defined as follows:

- The time complexity of Kmeans is O(N x k x t) where N, k, and t correspond to the number of feature vectors, number of clusters, and number of iterations respectively.
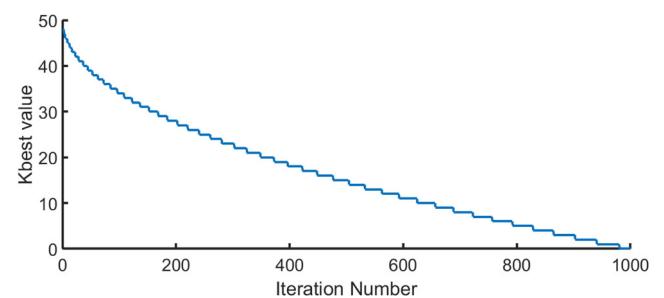
Fig. 7 Modified $Kbest$ over iterations

Table 1 The considered standard benchmark functions [27]

S.No.	Function	Equation	Range	O.V.	O.P.	Category
1.	Ackley	$F_1(X) = -20e^{-0.02\sqrt{d^{-1}\sum_{i=1}^{d}x_i^2}} - e^{d^{-1}\sum_{i=1}^{d}\cos(2\pi x_i)} + 20 + e$	[-35 to 35]	0	(0,...,0)	MM
2.	Alpine	$F_2(X) = \sum_{i=1}^{d}|x_i\sin(x_i) + 0.1x_i|$	[-10 to 10]	0	(0,...,0)	MM
3.	Brown	$F_3(X) = \sum_{i=1}^{d-1}(x_i^2)^{(x_{i+1}^2+1)} + (x_{i+1}^2)^{(x_i^2+1)}$	[-1 to 4]	0	(0,...,0)	UM
4.	Dixon and Price	$F_4(X) = (x_1-1)^2 + \sum_{i=2}^{d}i(2x_i^2 - x_{i-1})^2$	[-10 to 10]	0	$2^{\frac{-(2^i-2)}{(2^i)}}$, i=1,2,...,d	UM
5.	Griewank	$F_5(X) = 1 + \sum_{i=1}^{d}\frac{x_i^2}{4000} - \prod_{i=1}^{d}\cos(\frac{x_i}{\sqrt{i}})$	[-600 to 600]	0	(0,...,0)	MM
6.	Pathological	$F_6(X) = \sum_{i=1}^{d-1}\left(0.5 + \frac{\sin^2\sqrt{100x_i^2+x_{i+1}^2}-0.5}{1+0.001(x_i^2-2x_ix_{i+1}+x_{i+1}^2)^2}\right)$	[-100 to 100]	0	(0,...,0)	MM
7.	Quartic	$F_7(X) = \sum_{i=1}^{d}ix_i^4$	[-1.28 to 1.28]	0	(0,...,0)	UM
8.	Rosenbrock's	$F_8(X) = \sum_{i=1}^{d-1}[100(x_{i+1}-x_i^2)^2 + (x_i-1)^2]$	[-30 to 30]	0	(1,...,1)	UM
9.	Rosenbrock and Yang's	$F_9(X) = \sum_{i=1}^{d-1}\left[100\epsilon_i(x_{i+1}-x_i^2)^2 + (x_i-1)^2\right]$	[-30 to 30]	0	(1,...,1)	UM
10.	Rotated Hyper-Ellipsoid	$F_{10}(X) = \sum_{i=1}^{d}\sum_{j=1}^{i}x_j^2$	[-65.536 to 65.536]	0	(0,...,0)	UM
11.	Schumer Steiglitz	$F_{11}(X) = \sum_{i=1}^{d}x_i^4$	[-100 to 100]	0	(0,...,0)	UM
12.	Schwefel2	$F_{12}(X) = \sum_{i=1}^{d}\left(\sum_{j=1}^{i}x_j\right)^2$	[-65.536 to 65.536]	0	(0,...,0)	UM
13.	Schwefel3	$F_{13}(X) = \sum_{i=1}^{d}|x_i| + \prod_{i=1}^{d}|x_i|$	[-10 to 10]	0	(0,...,0)	MM
14.	Schwefel4	$F_{14}(X) = \max_i(|x_i| : i \in \{1,\cdots,d\})$	[-100 to 100]	0	(0,...,0)	UM
15.	Step	$F_{15}(X) = \sum_{i=1}^{d}(\lfloor|x_i|\rfloor)$	[-100 to 100]	0	(0,...,0)	UM
16.	Trigonometric	$F_{16}(X) = \sum_{i=1}^{d}[d - \sum_{j=1}^{d}\cos x_j + i(1-\cos(x_i) - \sin(x_i))]^2$	[0 to pi]	0	(0,...,0)	MM
17.	Zakharov	$F_{17}(X) = \sum_{i=1}^{d}x_i^2 + (\frac{1}{2}\sum_{i=1}^{d}ix_i)^2 + (\frac{1}{2}\sum_{i=1}^{d}ix_i)^4$	[-5 to 10]	0	(0,...,0)	MM

O.V.: Optimal Value; O.P.: Optimal Position; UM : Uni-Modal; MM : Multi-Modal

Table 2 Description of considered real-parameter single objective optimization problems of CEC, 2013 [78]

Sr. No.	Function	Range	Optimal value	Category
C_1	Sphere	[-100 to 100]	-1400	UM
C_2	Rotated High Conditioned Elliptic	[-100 to 100]	-1300	UM
C_3	Rotated Bent Cigar	[-100 to 100]	-1200	UM
C_4	Rotated Discus	[-100 to 100]	-1100	UM
C_5	Different Powers	[-100 to 100]	-1000	UM
C_6	Rotated Rosenbrock	[-100 to 100]	-900	MM
C_7	Rotated Schaffers F7	[-100 to 100]	-800	MM
C_8	Rotated Ackley	[-100 to 100]	-700	MM
C_9	Rotated Weierstrass	[-100 to 100]	-600	MM
C_{10}	Rotated Griewank	[-100 to 100]	-500	MM
C_{11}	Rastrigin	[-100 to 100]	-400	MM
C_{12}	Rotated Rastrigin	[-100 to 100]	-300	MM
C_{13}	Non-Continuous Rotated Rastrigin	[-100 to 100]	-200	MM
C_{14}	Schwefel	[-100 to 100]	-100	MM
C_{15}	Rotated Schwefel	[-100 to 100]	100	MM
C_{16}	Rotated Katsuura	[-100 to 100]	200	MM
C_{17}	Lunacek Bi_Rastrigin	[-100 to 100]	300	MM
C_{18}	Rotated Lunacek Bi_Rastrigin	[-100 to 100]	400	MM
C_{19}	Expanded Griewank plus Rosenbrock	[-100 to 100]	500	MM
C_{20}	Expanded Scaffer F6	[-100 to 100]	600	MM
C_{21}	CP 1 (n=5,Rotated)	[-100 to 100]	700	CP
C_{22}	CP 2 (n=3,Unrotated)	[-100 to 100]	800	CP
C_{23}	CP 3 (n=3,Rotated)	[-100 to 100]	900	CP
C_{24}	CP 4 (n=3,Rotated)	[-100 to 100]	1000	CP
C_{25}	CP 5 (n=3,Rotated)	[-100 to 100]	1100	CP
C_{26}	CP 6 (n=5,Rotated)	[-100 to 100]	1200	CP
C_{27}	CP 7 (n=5,Rotated)	[-100 to 100]	1300	CP
C_{28}	CP 8 (n=5,Rotated)	[-100 to 100]	1400	CP

UM : Unimodal; MM : Multimodal; CP : Composition

- As IGSA is a variant of GSA, the time complexity is similar to GSA which is O(P^2) [77], where P is the population size.
- The considered objective function has the computation complexity as O($N \times k$).

Further, each individual of KIGSA-C method is initialized with Kmeans and updated according to IGSA based on the defined objective function. Therefore, the time complexity of the proposed method is defined as O(N x k x $t + P^2 + N$ x k).

5 Experimental results

The experimental evaluation is conducted in two sections. Section 5.1 performs an extensive analysis of the proposed variant against recent metaheuristic algorithms. Two sets of benchmark functions, namely Standard benchmark functions ($F_1 - F_{17}$) and IEEE Congress on Evolutionary Computation (CEC), 2013 benchmark functions ($C_1 - C_{28}$), are considered which include unimodal, multimodal, and real parameter single-objective optimization problems of IEEE Congress on Evolutionary Computation (CEC), 2013. Section 5.2 studies the efficiency of the proposed clustering method over three publicly available medical chest image datasets for CoVID19, namely X-ray, CT-scans, and Ultrasound images. All experiments are simulated using a computer with a 2.35 GHz Intel Core i5 processor and 16 GB of RAM with Matlab 2017a.

5.1 Performance analysis of IGSA

Table 1 describes the first set (S_1) of benchmark functions consisting of ($F_1 - F_{17}$) functions [27] along with their definitions, range of features, global minimum fitness, optimal position values, and categories. Moreover, to validate the robustness, the second set (S_2) contains ($C_1 - C_{28}$) real-parameter single-objective unconstrained optimization functions [78] which are briefed in Table 2. The performance has been evaluated and statistically analyzed in terms of mean fitness value, Friedman test, and box-plot. To perform the comparative analysis, the new variant have been compared with standard GSA and nine variants of GSA, namely OGSA [50], mDGSA [61], GGSA [56], PGSA [59], MGSA(I) [57], MGSA(II) [58], EGSA(I) [51], EGSA(II) [52], and EGSA(III) [53]. The comparison also includes the performance results with three recent metaheuristic algorithms, namely modified particle swarm optimization (MPSO) [79], shuffled differential evolutionary (SDE) [80], and spiral biogeography based optimizer (SBBO) [81]. Moreover, the algorithms are evaluated over 10, 30, 50, and 90 dimensions for

each benchmark function. 30 run of each experiment is conducted to minimize the interference [82]. Table 3 details the parameter settings of all the considered algorithms which are taken from their respective literature. The parameter values of the proposed algorithm have been decided empirically by testing its performance on different parameter values of standard GSA algorithm.

Tables 4 and 5 tabulate the mean fitness values of the considered algorithms for S_1 set ($F_1 - F_{10}$) and ($F_{11} - F_{17}$) respectively. Furthermore, Tables 6, 7, and 8 show results on the S_2 set ($C_1 - C_{10}$), ($C_{11} - C_{20}$), and ($C_{21} - C_{28}$) respectively. In tables, best values are made bold. It can be observed that the IGSA has shown better results comparatively. On S_1 benchmark functions, IGSA obtained superior results on 53%, 71%, 59%, and 65% of 17 problems for each 10, 30, 50, and 90 dimensions respectively. While on the S_2 problems, IGSA outperformed compared algorithms on 54%, 61%, 50%, and 58% out of 28 problems on the respective dimensions. Thus, it can be seen that IGSA attains better trade-off between exploration and exploitation on different complexities functions.

To validate the IGSA statistically, Friedman's test [83] has been conducted between IGSA and considered algorithms. Friedman's test is a non-parametric statistical test and has been performed by considering the mean fitness values over 30 runs for each benchmark function in the S_1 and S_2 sets and results are presented in Tables 9 and 10 for each considered dimension. Generally, Friedman's test considers two hypotheses, namely null hypotheses and alternative hypotheses. The null hypothesis (H0) refers to that there is no significant difference among the samples

Table 3 Parameter settings of the considered algorithms

Parameter	Value
Number of runs	30
Population size (P)	50
Maximum iterations	1000
Number of dimensions ($Dims.$)	10, 30, 50, 90
MPSO	
Inertial Constant (w)	0.5
Congnitive Constant (c_1)	0.6
Social Constant (c_2)	0.4
SDE	
Weighting Factor (F)	0.3
Crossover Constant (CR)	0.7
SBBO	
Habitat modification probability	0.8
Immigration probability	0.7
Mutation probability	0.005
GSA and its variants	
Gconstant (G_0)	100

Table 4 Comparative analysis of existing and new algorithms for mean fitness values over 30 runs on the benchmark functions ($F_1 - F_{10}$) for different dimensions

Fn.	D	MPSO	SDE	SBBO	GSA	OGSA	mDGSA	GGSA	PGSA	MGSA(I)	MGSA(II)	EGSA(I)	EGSA(II)	EGSA(III)	LKGSA	CKGSA	EKGSA	IGSA
F_1	10	2.194E-44	4.423E-28	1.688E-12	7.608E-19	3.318E-18	6.872E-19	7.338E-19	7.961E+01	1.557E-20	1.078E-15	7.983E-23	1.962E+00	1.866E-23	7.222E-19	7.533E-19	5.923E-19	**5.655E-52**
	30	2.245E-14	2.464E-16	2.068E-02	1.275E-08	5.886E-17	9.940E-18	1.021E-03	3.804E+01	2.190E-19	1.089E-14	1.059E+02	2.194E+01	1.571E-21	9.795E-19	9.620E-18	3.380E-03	**2.846E-27**
	50	2.572E-05	3.198E-05	1.367E+01	1.494E-04	1.765E+03	7.428E-17	7.407E+00	3.988E+01	2.213E+03	7.342E-14	6.736E-106	5.906E-14	3.257E-18	1.767E+04	1.825E-16	1.490E-11	**1.341E-171**
	90	2.276E-01	4.663E+00	1.166E+02	1.575E+00	1.873E+04	3.558E-16	8.127E+03	1.265E+03	2.443E+04	1.609E-03	4.433E-104	2.769E+02	7.100E+00	7.322E-15	1.768E-15	7.557E-09	**1.610E-165**
F_2	10	9.679E-11	3.239E-15	1.304E-07	2.577E-09	5.316E-09	2.483E-09	3.096E-02	4.986E-02	3.543E-10	7.807E-08	1.452E-18	3.661E+00	1.242E-11	2.435E-09	2.369E-09	1.826E-12	**6.526E-19**
	30	3.061E-21	9.289E-46	3.786E-02	3.097E+01	2.617E+01	1.482E-08	1.055E-01	1.446E-01	2.219E-09	4.354E-07	8.005E+00	2.702E+01	1.865E-10	1.612E-08	1.557E-08	2.455E-01	**9.899E-221**
	50	6.716E-02	5.974E-04	1.530E+00	2.671E+00	4.795E+01	5.600E-08	6.291E+00	3.180E+00	9.128E-02	1.338E-06	7.939E-57	5.209E+01	2.069E-04	5.638E-03	7.367E-08	3.955E-05	**3.223E-109**
	90	3.333E+00	8.105E-01	6.325E+00	9.292E+00	1.366E+02	3.899E-03	1.035E-01	3.053E+01	2.739E+01	6.665E-01	2.017E-55	1.127E+02	2.939E+01	2.424E+00	3.188E-02	1.216E-02	**5.903E-107**
F_3	10	2.298E-53	2.941E+02	1.153E-04	1.396E-18	1.118E-17	1.482E-18	2.192E-03	2.254E-02	5.068E-20	2.414E-15	**0.000E+00**	6.037E+00	7.869E-23	1.184E-18	1.328E-18	4.757E-69	**8.682E-78**
	30	8.822E-04	6.959E+03	1.213E+01	2.743E-01	1.614E+03	2.792E-03	1.473E+02	8.260E+02	8.878E-18	1.032E-13	5.098E+02	5.512E+02	1.448E-01	9.152E-17	5.188E-17	2.130E-02	**8.408E-19**
	50	3.753E+02	8.962E+04	1.179E+03	8.053E+04	1.400E+04	1.478E+02	5.786E+01	1.073E+03	2.429E+04	3.684E+03	4.628E+03	3.065E+03	9.172E+02	1.144E+05	4.307E+02	3.843E+02	**1.778E-47**
	90	5.454E+03	3.120E+05	1.418E+04	5.263E+05	7.851E+05	6.288E+02	5.555E+01	3.797E+03	8.216E+04	1.318E+04	2.575E+04	1.017E+04	3.846E+03	5.109E+05	2.949E+03	2.406E+03	**5.849E-37**
F_4	10	1.072E-61	1.066E-11	2.453E-04	5.846E-10	1.281E-09	6.203E-10	1.569E-09	1.123E-02	1.077E-10	2.140E-08	1.636E-229	7.704E-01	3.448E-12	5.734E-10	5.944E-10	8.839E-06	**2.067E-231**
	30	8.905E-03	7.202E-07	3.277E-01	1.043E-00	1.983E+00	1.875E-09	1.415E-02	3.383E-01	4.389E-10	6.874E-08	5.896E+00	1.825E+00	1.142E-10	2.224E+00	2.032E-09	3.656E-02	**8.346E-216**
	50	1.963E+00	2.325E+01	2.013E+00	4.139E+01	1.665E+01	3.394E-05	9.813E-01	8.988E+00	4.170E+01	1.015E-02	**2.058E-33**	6.923E+00	3.641E+00	2.797E-01	1.206E+00	1.455E+00	8.185E+00
	90	5.798E+00	7.416E+01	4.542E+00	5.669E+01	1.897E+01	1.528E+00	8.832E-01	1.226E-01	5.076E-01	5.627E+00	1.404E+01	1.106E+01	1.063E+01	4.946E+01	7.839E+00	7.741E+00	**1.321E-22**
F_5	10	1.536E+00	5.428E+03	3.908E+00	4.397E-02	1.982E-01	4.363E-01	1.309E+01	1.794E+06	8.136E-01	5.892E-03	8.700E+00	3.137E+02	1.304E-02	**2.479E-13**	4.212E-05	1.290E-01	1.121E-01
	30	3.334E+01	2.800E+01	5.907E+01	5.180E+01	4.031E+01	2.040E+01	2.415E+01	3.727E+05	2.924E+01	1.991E+01	2.971E+01	7.006E+01	1.964E+01	2.815E+00	1.701E+00	2.056E+00	**1.051E+00**
	50	1.220E+02	1.866E+02	5.040E+02	4.706E+02	1.104E+06	4.625E+01	4.829E+02	4.719E+02	2.594E+04	5.214E+01	4.888E+01	2.938E+04	6.427E+01	1.111E+02	4.475E+02	**4.419E+01**	3.896E+05
	90	6.215E+02	8.226E+02	2.088E+03	8.732E+02	1.675E+06	8.642E+01	5.474E+02	7.587E+02	1.686E+06	7.344E+02	8.886E+01	1.321E+05	1.055E+03	5.388E+04	**8.478E+01**	1.263E+02	2.019E+06
F_6	10	9.547E-33	9.547E-33	3.021E-12	7.815E-19	3.832E-18	7.177E-19	7.548E-19	3.885E-04	1.706E-20	1.105E-15	6.041E-02	2.032E+00	1.813E-23	6.052E-19	7.175E-19	3.975E-28	**6.050E-37**
	30	2.521E-32	**5.872E-27**	1.798E-02	1.388E-08	5.550E-17	1.067E-17	1.117E-03	2.007E-03	2.688E-19	1.027E-14	1.294E+02	2.110E+01	2.096E-21	1.026E-17	8.892E-18	2.691E-03	2.988E-01
	50	1.115E-04	3.828E-05	1.294E+01	4.016E-02	1.026E+03	6.454E-17	5.859E+00	1.242E+01	2.785E+03	7.382E-14	1.466E+00	5.702E+01	1.584E+02	**3.507E-18**	1.024E-16	1.255E-11	2.237E+02
	90	3.622E-01	4.913E+00	1.160E+02	4.727E-01	1.046E+04	1.478E-01	8.935E+00	1.068E+03	2.573E+04	8.140E-04	1.344E+01	3.287E+02	1.153E-01	7.707E+04	1.734E-15	4.813E-09	**4.612E-16**
F_7	10	4.452E-04	1.090E-03	1.549E-04	2.674E-03	7.153E-03	1.290E-03	3.516E-03	2.394E-01	6.742E-04	4.238E-03	**4.559E-06**	3.761E-01	6.146E-04	8.918E-03	5.951E-03	1.153E-02	4.924E-04
	30	8.753E-03	4.689E-03	7.869E-04	6.930E-04	8.450E-02	8.919E-03	5.467E-05	1.071E-02	6.903E-03	2.164E-02	7.807E-02	2.953E-03	3.365E-03	7.968E-02	4.351E-02	1.092E-01	**7.322E-06**
	50	2.997E-01	7.953E-02	9.287E-03	1.380E-03	5.523E+00	2.292E-02	7.384E-03	9.789E-03	1.209E-01	7.888E-02	7.986E-02	1.717E+02	4.101E-02	3.676E-01	1.269E-01	1.143E-01	**3.387E-05**
	90	6.485E+02	3.938E+02	3.376E-02	7.628E+00	4.736E+01	7.379E+02	1.546E+02	1.356E+02	8.546E-01	4.730E+01	4.765E-01	7.552E+02	3.581E+01	**3.263E-01**	3.376E-01	3.726E-01	1.821E+02
F_8	10	5.111E+02	1.204E+03	1.445E+03	5.753E+02	1.012E+03	5.692E+02	2.083E+03	5.041E+02	8.581E+02	4.372E+02	4.823E+02	4.200E+02	**3.919E+02**	5.116E+02	5.237E+02	5.253E+02	2.095E+03
	30	4.810E+03	1.047E+04	6.318E+03	3.445E+03	6.910E+02	6.310E+02	1.046E+04	6.178E+04	5.053E+03	1.604E+03	1.358E+03	4.368E+03	2.270E+03	7.551E+02	5.271E+02	5.443E+02	**3.915E+02**
	50	9.030E+03	1.116E+04	1.115E+04	1.633E+04	**6.094E+02**	1.190E+03	1.796E+04	1.491E+04	7.522E+03	1.874E+03	1.493E+03	8.114E+03	1.811E+03	1.606E+03	1.546E+03	1.764E+03	1.166E+03
	90	1.568E+04	1.518E+04	1.990E+04	3.401E+04	**1.253E+03**	2.455E+03	3.132E+03	2.375E+04	1.122E+04	3.713E+03	2.652E+03	1.615E+04	3.307E+03	2.762E+03	2.732E+03	2.485E+03	2.304E+03
F_9	10	1.405E+00	1.927E+01	7.921E+01	2.965E+00	2.020E+01	5.658E-01	3.118E+00	1.146E-20	5.697E+00	3.609E+00	5.909E+00	3.638E+01	2.556E+00	1.218E+01	5.443E+00	1.175E+01	**1.024E+00**
	30	2.840E+01	3.387E-10	3.275E+01	6.666E+01	1.025E+02	1.266E+00	1.071E+01	5.496E+12	3.175E+01	1.972E+01	1.755E+02	2.216E+02	1.393E+01	5.147E+01	2.189E+01	1.133E+01	**1.010E+00**
	50	1.110E+02	2.002E+02	7.090E+01	2.357E+01	1.757E+01	9.045E+01	9.744E+01	6.979E+08	6.892E+01	3.781E+01	3.148E+01	4.480E+02	3.012E+01	1.085E+02	5.780E+01	4.622E+01	**1.322E+01**
	90	3.393E+02	5.874E+02	1.848E+02	**1.218E+01**	4.436E-02	3.075E+00	3.468E+02	2.614E+07	1.689E+02	7.697E+01	9.768E+01	8.922E+02	6.720E+01	1.565E+02	1.328E+02	8.349E+01	5.727E+02
F_{10}	10	4.371E-15	3.948E-02	3.800E-01	1.252E-09	5.879E-03	1.255E-02	2.833E-02	1.416E+00	1.906E-10	4.256E-08	**8.882E-16**	3.126E+00	5.940E-12	1.188E+00	1.167E+00	4.371E-15	3.257E-15
	30	1.187E-14	7.994E-15	3.444E-02	2.035E+00	1.395E-01	2.303E-01	2.341E+00	3.030E+00	4.362E-10	7.728E-08	5.789E+00	4.779E+00	3.357E-11	2.323E+00	2.451E-09	4.702E-02	**8.882E-16**
	50	2.247E-01	1.346E-03	1.221E+00	4.764E-15	1.028E+01	5.094E-09	2.764E+00	5.140E+00	9.726E+00	1.483E-07	5.065E+00	5.569E+00	1.153E-09	5.884E+00	**8.882E-16**	1.517E-06	7.306E+00
	90	1.822E+00	7.202E-01	2.752E+00	4.118E-15	1.004E+01	8.161E-09	2.903E+00	1.226E+00	1.602E+01	7.269E-01	3.124E+00	6.132E+00	3.873E-01	8.052E+00	1.923E-08	3.126E-01	**8.882E-16**

Bold font : Best value

Table 5 Comparative analysis of existing and new algorithms for mean fitness values over 30 runs on the benchmark functions ($F_{11} - F_{17}$) for different dimensions

Fn.	D	MPSO	SDE	SBBO	GSA	OGSA	mDGSA	GGSA	PGSA	MGSA(I)	MGSA(II)	EGSA(I)	EGSA(II)	EGSA(III)	LKGSA	CKGSA	EKGSA	IGSA
F_{11}	10	1.005E-01	1.558E-01	2.723E-02	3.043E-03	4.225E-02	3.332E-03	6.363E-04	4.836E+10	2.580E-01	3.813E-03	8.313E-04	2.409E-01	3.525E-03	1.073E+00	4.637E-03	7.701E-03	**2.081E-05**
	30	1.499E-02	9.350E-02	6.302E-02	1.253E-02	1.906E+02	5.606E+02	6.430E-01	2.383E+59	1.024E+00	1.413E-16	1.064E+00	7.192E-01	1.793E-03	1.708E+01	2.408E+01	7.708E-04	**1.398E-05**
	50	7.391E-03	1.713E-04	1.117E+00	4.755E+01	1.193E+03	1.620E+01	8.643E-01	1432E+118	7.789E+01	5.145E-03	1.810E+00	1.759E+01	1.594E+00	9.146E+02	4.379E+01	1.532E+01	**2.902E+00**
	90	1.415E-02	9.958E-01	2.038E+00	1.290E-02	2.226E+03	5.030E+01	7.315E-01	1.338E+125	4.412E+02	5.751E-02	1.388E-02	4.393E+01	4.509E+01	1.869E+03	2.779E+02	5.304E+01	**2.902E+00**
F_{12}	10	1.267E-24	7.317E-02	1.603E-14	1.548E-20	6.559E-02	1.585E-01	2.063E-05	2.472E+11	3.129E-22	2.582E-17	7.002E-03	1.266E-01	3.473E-25	7.185E-01	1.222E-20	4.188E-06	**4.712E-32**
	30	1.687E-32	**1.571E-32**	4.435E-05	6.047E+00	4.757E+00	3.769E-02	8.548E-06	8.837E+07	4.712E-02	7.861E-17	4.891E+00	6.155E-01	1.174E-23	3.315E-01	5.638E-20	9.443E-03	9.343E-03
	50	**2.791E-07**	2.078E-05	2.227E-02	3.438E-03	4.466E+02	1.131E-02	2.350E-02	1.160E+01	1.377E+01	2.262E-02	7.833E-01	5.900E+00	1.585E-01	8.581E+00	4.523E-02	5.089E-02	8.390E+00
	90	4.204E-01	1.213E+01	2.114E-01	1.083E+01	6.562E+03	2.207E-02	1.236E-02	4.203E+02	5.484E+06	1.698E+00	1.058E+00	1.805E+01	1.850E+00	1.554E+04	6.871E-01	6.984E-01	**5.983E-03**
F_{13}	10	**1.350E-32**	3.232E-03	1.290E-13	6.896E-20	1.107E-05	8.087E-20	9.101E-05	1.359E+291	1.591E-21	1.198E-16	2.425E-02	3.393E-01	6.760E-24	7.081E-20	1.547E-04	2.374E-04	1.763E-24
	30	1.998E-03	7.514E-02	5.789E-04	4.908E-03	6.169E+01	9.187E-19	1.355E-04	1.495E+208	2.554E-20	1.115E-15	3.493E+03	6.942E+00	1.565E-22	3.139E-01	9.989E-04	2.293E-03	**1.350E-32**
	50	3.020E-03	9.832E-05	5.564E-01	2.215E-01	5.756E-04	1.952E+01	5.690E-01	3.694E+53	3.966E+02	1.032E-01	3.158E-06	4.011E+01	1.748E+00	9.468E+01	1.998E-03	1.131E-01	**5.838E-18**
	90	1.013E+00	1.105E+02	4.750E+00	7.398E-01	1.922E+06	1.719E+02	6.212E-01	4.444E+47	2.807E+07	4.167E+01	8.985E+00	8.097E+02	5.746E+01	1.400E+06	1.517E+00	**9.989E-04**	2.329E-01
F_{14}	10	1.162E+00	2.347E-01	3.081E+00	5.412E-01	6.463E-01	3.933E+00	3.553E-01	3.880E+02	1.996E-03	3.033E-02	4.571E-01	1.953E-03	4.873E-01	**1.872E-03**	5.062E-01	6.337E-01	2.141E-02
	30	1.346E+00	1.996E-02	3.220E+00	1.996E+00	4.507E-01	4.652E+00	1.902E-01	3.065E+02	1.996E-03	5.919E-03	1.955E+00	**1.857E-03**	4.520E-01	4.863E+00	2.043E-01	9.558E-01	4.533E-01
	50	8.085E-01	1.996E-02	3.047E+00	2.137E+00	2.328E+00	2.168E+00	1.920E+00	1.424E+02	3.620E-01	5.458E-01	2.166E+00	4.014E-02	1.799E+00	4.785E+00	**1.996E-03**	3.422E+00	3.482E+00
	90	5.420E-01	**1.996E-03**	3.817E+00	5.420E-01	3.003E+00	2.523E+00	2.283E+00	1.404E+02	3.015E+00	6.812E-01	1.131E+00	1.969E-02	1.172E+00	3.990E+00	2.520E+00	3.683E+00	**1.996E-03**
F_{15}	10	2.207E-04	1.022E-03	9.385E-04	9.122E-04	1.452E-03	1.014E-04	1.404E-04	2.874E+04	2.737E-05	6.199E-04	3.291E-04	6.993E-04	3.301E-04	2.894E-04	4.981E-04	**7.486E-06**	2.717E-05
	30	3.832E-04	1.021E-04	2.070E-03	2.177E-03	8.834E-04	1.694E-04	1.171E-03	3.364E+04	**7.486E-06**	5.651E-04	1.648E-03	7.827E-04	3.252E-04	1.009E-03	4.355E-04	1.963E-04	3.123E-04
	50	4.313E-04	3.025E-04	2.365E-04	3.962E-04	4.012E-03	2.842E-04	3.315E-04	8.759E+02	1.425E-04	1.458E-04	8.265E-04	1.145E-03	8.110E-04	1.349E-03	8.518E-04	4.527E-04	**7.486E-06**
	90	5.023E-04	3.975E-04	3.154E-04	3.000E-04	3.278E-04	1.993E-04	4.154E-04	8.725E+02	2.493E-04	1.595E-04	5.848E-04	1.404E-04	7.156E-04	1.730E-03	8.111E-04	2.636E-03	**7.486E-06**
F_{16}	10	2.845E-05	2.845E-05	2.845E-05	2.845E-05	3.757E-05	2.845E-05	2.840E-05	5.362E+04	2.845E-05	2.845E-05	2.654E-04	1.642E-04	2.845E-05	2.845E-05	**2.625E-05**	2.786E-05	2.845E-05
	30	2.845E-05	2.845E-05	2.845E-05	2.845E-05	2.845E-05	2.845E-05	2.840E-05	2.271E+04	2.845E-05	2.845E-05	2.645E-05	1.110E-04	2.845E-05	2.845E-05	2.845E-05	2.774E-05	**2.585E-05**
	50	2.845E-05	2.845E-05	2.845E-05	2.845E-05	1.986E-04	2.845E-05	2.811E-05	3.201E+03	2.845E-05	2.845E-05	9.227E-04	7.736E-04	2.845E-05	2.845E-05	2.845E-05	2.845E-05	**1.698E-05**
	90	2.845E-05	2.845E-05	2.845E-05	2.845E-05	2.142E-04	2.845E-05	2.830E-05	1.197E+03	2.845E-05	2.845E-05	1.338E-03	7.212E-04	2.845E-05	2.845E-05	2.845E-05	2.845E-05	**1.867E-05**
F_{17}	10	7.529E-14	7.771E-14	5.294E-01	7.425E-14	7.597E-14	2.740E+00	1.380E-07	4.503E+06	7.652E-14	5.850E-14	1.846E-02	5.441E-03	7.653E-14	7.476E-14	7.753E-14	4.018E-05	**3.920E-14**
	30	7.828E-14	7.864E-14	2.455E+00	**2.701E-14**	6.823E-14	9.229E-01	1.382E-07	2.451E+06	7.840E-14	5.955E-14	1.896E-02	4.981E-03	7.788E-14	7.723E-14	7.788E-14	4.513E-05	2.505E-02
	50	6.363E-14	7.860E-14	6.968E-14	1.286E-06	6.665E-14	1.369E+00	7.697E-07	5.281E+05	7.529E-14	4.413E-14	7.616E-02	2.737E-02	7.659E-14	7.485E-14	7.485E-14	6.052E-14	**4.170E-14**
	90	7.820E-14	7.868E-14	6.403E-14	1.536E-06	7.327E-14	1.703E+00	9.104E-07	6.374E+04	7.642E-14	1.870E-06	8.080E-02	3.346E-02	7.687E-14	6.843E-14	**4.203E-14**	5.555E-14	5.441E-02

Bold font : Best value

Table 6 Comparative analysis of existing and new algorithms for mean fitness values over 30 runs on the CEC2013 benchmark functions ($C_1 - C_{10}$) for considered dimensions

Fn.	D	MPSO	SDE	SBBO	GSA	OGSA	mDGSA	GGSA	PGSA	MGSA(I)	MGSA(II)	EGSA(I)	EGSA(II)	EGSA(III)	LKGSA	CKGSA	EKGSA	IGSA
C_1	10	4.012E-14	1.490E-06	2.297E-10	1.946E+00	1.405E+01	5.631E-10	2.962E-11	2.867E-04	3.336E-10	1.603E-09	3.948E-01	2.225E+00	4.703E-10	1.929E-09	7.368E-10	1.471E-10	**3.737E-12**
	30	4.961E-13	2.067E-13	6.618E-02	1.447E-13	2.274E-13	1.240E-13	5.085E+04	3.449E+03	1.860E-13	3.610E+04	1.184E+00	2.293E+01	2.067E-13	3.130E+03	2.274E-13	3.927E-13	**1.174E-13**
	50	1.946E+00	3.211E-05	1.379E+01	1.131E+04	7.066E+04	2.786E+04	8.193E+04	4.282E+04	9.652E+03	5.545E+03	1.335E+04	9.978E+03	1.046E+04	7.393E+04	1.356E+03	**6.408E-13**	6.615E-13
	90	4.126E+02	3.124E+00	1.153E+02	7.544E+04	1.984E+05	9.752E+04	1.665E+05	1.254E+05	6.804E+04	4.183E+01	6.602E+04	7.337E+04	6.957E+04	1.851E+05	4.803E+04	6.202E+04	**1.199E-12**
C_2	10	3.155E+05	2.124E+04	1.213E+05	9.890E+05	4.974E+06	8.458E+05	3.158E+06	9.454E+05	7.785E+04	1.889E+05	5.528E+06	3.753E+06	8.316E+05	3.988E+05	8.907E+03	**4.940E+03**	1.671E+06
	30	1.519E+07	7.604E+07	3.597E+06	6.347E+06	2.757E+07	4.733E+06	1.665E+09	3.601E+07	1.982E+08	5.647E+08	2.400E+07	1.923E+07	5.694E+06	7.115E+07	6.894E+06	2.679E+06	**1.206E+02**
	50	8.546E+07	5.625E+08	1.538E+08	1.037E+08	3.369E+09	2.936E+08	3.651E+09	1.085E+09	5.423E+08	2.269E+07	1.755E+08	1.407E+08	9.684E+07	2.874E+09	6.675E+07	6.372E+07	**2.009E+06**
	90	4.048E+07	5.801E+08	1.304E+07	1.286E+09	1.348E+10	2.106E+09	8.808E+09	3.988E+09	1.700E+09	3.987E+07	1.867E+09	1.521E+09	1.071E+09	8.576E+09	6.986E+08	9.497E+08	**4.543E+05**
C_3	10	2.458E+05	3.740E+07	2.221E+07	4.837E+07	1.810E+09	2.707E+08	4.244E+07	4.115E+08	6.689E+06	2.237E+05	2.583E+08	2.975E+08	6.448E+07	5.242E+07	2.982E+06	3.003E+04	**1.655E+00**
	30	2.738E+08	1.711E+08	2.747E+08	5.335E+09	3.737E+10	3.440E+09	1.146E+20	7.077E+10	1.777E+12	1.284E+16	1.652E+10	7.411E+09	3.681E+09	1.681E+14	3.310E+08	**7.253E+06**	1.601E+07
	50	1.614E+10	4.866E+10	1.090E+09	1.503E+11	1.602E+23	3.113E+11	1.035E+17	1.171E+14	4.851E+11	7.402E+09	7.626E+11	3.842E+11	9.275E+10	1.216E+17	3.181E+10	5.191E+10	**1.166E+08**
	90	3.856E+10	4.857E+10	3.807E+09	7.820E+17	3.186E+28	1.990E+17	5.155E+21	5.265E+19	5.169E+18	2.214E+12	3.009E+18	1.008E+18	1.388E+18	3.365E+24	6.103E+13	4.751E+15	**2.429E+08**
C_4	10	5.083E+02	1.366E+04	1.755E+04	1.664E+04	1.788E+04	1.766E+04	8.524E+03	1.812E+04	4.514E+01	1.250E+04	1.654E+04	1.021E+04	1.645E+04	1.235E+04	1.826E+04	**4.904E-13**	8.549E+03
	30	7.590E+03	6.337E+04	1.091E+03	7.257E+04	6.896E+04	6.745E+04	6.805E+04	7.045E+04	2.766E+04	6.276E+04	6.710E+04	6.490E+04	6.703E+04	5.939E+04	6.637E+04	6.636E+04	**2.043E-08**
	50	7.098E+04	1.748E+05	5.558E+04	9.448E+04	4.250E+07	8.937E+04	1.311E+05	9.611E+04	1.318E+05	9.764E+04	9.472E+04	8.905E+04	9.443E+04	3.178E+05	9.823E+04	9.405E+04	**3.317E+02**
	90	1.426E+05	2.165E+05	3.798E+04	1.773E+05	1.255E+09	1.725E+05	2.584E+05	1.734E+05	2.391E+05	1.833E+05	1.818E+05	1.794E+05	1.707E+05	6.012E+06	1.656E+05	1.644E+05	**4.785E+02**
C_5	10	9.362E-14	3.680E-04	3.431E-06	2.574E-05	5.797E-04	2.669E-05	3.324E-08	3.761E-02	7.074E-04	1.765E-10	2.013E+01	1.205E+01	2.581E+01	2.229E-15	1.627E-12	1.025E-13	**2.124E-15**
	30	2.478E-11	**1.137E-13**	1.303E-01	3.027E-10	2.390E-02	2.215E-10	3.325E+04	8.382E+02	1.571E-12	1.410E+04	6.122E+01	7.183E+01	5.147E-12	4.605E+02	9.302E-13	3.721E-13	8.165E-13
	50	6.146E+00	4.809E-03	4.986E+00	1.617E+03	1.637E+04	2.598E+03	2.556E+04	5.708E+03	1.517E+03	1.474E+02	2.394E+03	1.713E+03	1.474E+03	2.463E+02	3.313E+02	7.988E+02	**7.848E-09**
	90	2.335E+02	8.771E+00	3.723E+00	1.504E+04	9.193E+04	1.795E+04	8.689E+04	3.366E+04	1.376E+04	9.497E+02	2.106E+04	1.534E+04	1.415E+04	1.237E+05	4.609E+03	9.205E+03	**3.622E-08**
C_6	10	**6.173E+00**	9.765E+00	6.992E+00	4.352E+00	3.741E+01	3.696E+01	1.107E+01	2.599E+01	7.395E+00	9.494E+00	6.701E+01	4.830E+01	4.432E+01	2.129E+01	1.110E+01	7.507E+00	9.813E+00
	30	7.912E+01	2.463E+01	5.207E+01	7.848E+01	1.130E+02	5.116E+01	1.530E+04	3.880E+02	1.448E+03	6.651E+03	9.351E+01	7.238E+01	6.896E+01	1.253E+03	6.395E+01	**1.020E+01**	5.009E+01
	50	7.188E+01	4.791E+01	6.306E+01	6.613E+02	9.444E+03	1.798E+03	1.189E+04	3.806E+03	1.986E+03	8.448E+01	8.271E+02	7.057E+02	5.548E+02	9.467E+02	2.959E+02	3.668E+02	**4.450E+01**
	90	6.542E+02	4.446E+02	3.023E+02	1.286E+04	4.393E+04	1.812E+04	4.482E+04	2.634E+04	1.956E+04	7.724E+02	1.382E+04	1.326E+04	1.165E+04	5.544E+04	8.975E+03	9.927E+03	**2.068E+02**
C_7	10	3.355E+01	4.109E+04	5.373E+01	1.249E+01	7.010E+01	2.878E+01	1.525E+01	6.431E+01	1.930E+01	5.563E+00	1.940E+01	2.300E+01	1.122E+01	1.105E+01	6.289E+00	3.236E-01	**5.316E-06**
	30	4.055E+01	7.026E+01	1.126E+02	6.502E+01	1.371E+04	7.744E+01	1.583E+07	1.668E+06	1.017E+03	6.511E+04	7.509E+01	8.450E+01	6.233E+01	1.371E+05	6.473E+01	2.248E+01	**1.976E+01**
	50	1.376E+02	1.835E+02	1.260E+02	7.189E+02	3.096E+09	6.367E+03	2.881E+05	1.238E+05	6.975E+02	6.574E+01	1.052E+03	2.930E+02	1.927E+03	1.097E+05	2.723E+02	3.535E+02	**5.539E+01**
	90	1.322E+02	1.582E+02	1.212E+02	6.129E+05	3.850E+10	1.916E+06	7.451E+06	8.088E+06	2.547E+05	4.644E+02	8.082E+05	1.672E+05	1.039E+06	3.227E+07	2.661E+05	5.399E+05	**9.417E+01**
C_8	10	2.530E+01	2.332E+01	2.631E+01	2.434E+01	2.137E+01	3.534E+01	2.539E+01	3.331E+01	4.432E+01	3.133E+01	3.640E+01	2.733E+01	3.129E+01	2.135E+01	2.534E+01	2.235E+01	**2.019E+01**
	30	2.397E+01	4.198E+01	3.598E+01	3.399E+01	4.700E+01	3.298E+01	3.096E+01	3.496E+01	2.190E+01	2.295E+01	2.302E+01	2.397E+01	2.290E+01	2.399E+01	2.298E+01	2.599E+01	**2.084E+01**
	50	2.320E+01	3.220E+01	3.421E+01	3.522E+01	2.223E+01	2.322E+01	3.420E+01	3.321E+01	2.416E+01	2.222E+01	3.320E+01	2.520E+01	2.220E+01	3.020E+01	2.321E+01	2.419E+01	**2.110E+01**
	90	2.632E+01	3.130E+01	3.025E+01	2.264E+01	2.613E+01	**2.060E+01**	2.137E+01	2.118E+01	3.104E+01	2.978E+01	3.135E+01	2.836E+01	3.477E+01	2.335E+01	2.372E+01	2.490E+01	2.228E+01

Bold font : Best value

Table 7 Comparative analysis of existing and new algorithms for mean fitness values over 30 runs on the CEC2013 benchmark functions $(C_{11} - C_{20})$ for considered dimensions

Fn.	D	MPSO	SDE	SBBO	GSA	OGSA	mDGSA	GGSA	PGSA	MGSA(I)	MGSA(II)	EGSA(I)	EGSA(II)	EGSA(III)	LKGSA	CKGSA	EKGSA	IGSA
C_{11}	10	1.639E+00	2.246E+02	2.330E+00	1.781E+01	3.095E+01	1.694E+02	5.316E-01	1.311E+02	2.045E+01	3.524E+00	1.838E+01	2.394E+01	1.807E+01	5.437E+01	2.654E+01	6.067E+00	**1.951E-07**
	30	2.605E+01	1.809E+01	2.401E+01	2.743E+02	4.124E+02	6.797E+02	8.679E+02	6.946E+02	2.202E+02	7.034E+02	2.886E+02	3.808E+02	2.915E+02	4.636E+02	3.275E+02	4.838E+01	2.858E+01
	50	1.210E+02	1.988E+02	1.265E+02	6.524E+02	1.150E+02	8.774E+02	1.201E+02	8.097E+02	6.298E+02	1.308E+02	6.295E+02	8.160E+02	6.758E+02	1.222E+02	6.048E+02	6.288E+02	**9.894E+01**
	90	3.970E+02	5.762E+02	4.525E+02	1.786E+03	2.971E+02	2.115E+03	2.850E+03	2.163E+03	1.751E+03	4.241E+03	1.835E+03	2.143E+03	1.783E+03	3.445E+03	1.635E+03	**1.700E+02**	3.201E+02
C_{12}	10	1.344E+01	2.372E+02	1.957E+01	1.405E+01	3.149E+01	1.454E+02	9.753E+02	1.396E+02	1.816E+01	3.102E+02	1.495E+01	1.653E+01	1.414E+01	4.918E+01	**2.576E+00**	9.501E+01	1.325E+01
	30	1.000E+02	1.953E+02	1.073E+02	3.351E+02	4.551E+02	8.155E+02	8.827E+02	7.594E+02	3.491E+02	6.829E+02	3.291E+02	3.678E+02	3.398E+02	4.346E+02	4.261E+01	5.512E+01	**1.610E+01**
	50	4.038E+02	4.851E+02	2.169E+02	9.196E+02	1.574E+03	1.014E+03	1.331E+03	9.858E+03	8.130E+02	8.334E+02	9.277E+02	9.930E+02	9.077E+02	**6.847E+01**	4.031E+02	8.721E+02	1.352E+02
	90	7.192E+02	1.011E+03	6.338E+02	2.048E+03	3.275E+03	2.339E+03	3.090E+03	2.267E+03	2.093E+03	9.496E+02	2.132E+03	2.298E+03	2.044E+03	**3.546E+02**	1.247E+03	2.021E+03	3.861E+02
C_{13}	10	1.861E+01	2.604E+02	3.477E+01	3.244E+01	5.595E+01	1.611E+02	1.862E+02	1.567E+02	3.126E+01	5.813E+00	3.382E+01	3.148E+01	2.902E+01	**4.288E+00**	8.289E+01	1.632E+01	1.443E+01
	30	1.754E+02	2.002E+02	1.762E+02	4.514E+02	6.875E+02	8.922E+02	9.061E+02	8.809E+02	5.135E+02	6.651E+02	4.514E+02	4.098E+02	4.587E+02	5.883E+02	1.000E+02	1.142E+02	**4.273E+01**
	50	4.821E+02	4.757E+02	3.153E+02	1.089E+03	1.747E+03	1.288E+03	1.345E+03	1.241E+03	8.608E+02	**1.760E+02**	1.038E+03	9.983E+02	1.117E+03	1.230E+03	5.183E+02	1.130E+03	2.362E+02
	90	8.673E+02	9.931E+02	6.664E+02	2.384E+03	3.738E+03	2.732E+03	3.030E+03	2.747E+03	2.214E+03	9.501E+02	2.452E+03	2.363E+03	2.402E+03	3.571E+03	1.640E+03	2.411E+03	**5.762E+02**
C_{14}	10	9.271E+01	1.511E+03	3.067E+02	7.153E+02	1.253E+03	1.636E+03	1.708E+01	1.369E+03	7.925E+03	3.630E+03	7.567E+02	8.055E+02	6.917E+02	1.200E+03	4.267E+02	1.856E+02	**1.025E-01**
	30	8.069E+02	**7.542E+02**	1.198E+03	3.572E+03	4.913E+03	5.204E+03	6.919E+03	5.374E+03	3.096E+03	7.934E+03	3.546E+03	4.683E+03	3.576E+03	4.882E+03	2.867E+03	1.997E+03	2.080E+03
	50	3.746E+03	5.709E+03	3.509E+03	7.300E+03	9.768E+03	8.523E+03	1.475E+04	8.521E+03	6.629E+03	5.035E+03	8.004E+03	9.832E+03	7.497E+03	1.551E+03	6.318E+03	**7.156E+02**	3.375E+03
	90	1.095E+04	1.851E+04	1.094E+04	1.453E+04	2.133E+04	1.598E+04	2.836E+04	1.683E+04	1.653E+04	1.093E+04	1.581E+04	2.057E+04	1.499E+04	3.006E+04	1.261E+04	1.371E+04	**4.323E+03**
C_{15}	10	7.843E+02	1.298E+03	1.016E+03	4.395E+02	1.034E+03	1.063E+03	1.434E+03	9.626E+02	7.537E+02	2.054E+02	3.772E+02	4.566E+02	3.982E+02	8.454E+02	**1.884E+02**	6.314E+02	1.037E+03
	30	6.878E+03	7.509E+03	4.118E+03	3.417E+03	4.325E+03	4.374E+03	5.491E+03	4.842E+03	4.363E+03	7.513E+03	3.733E+03	4.495E+03	3.899E+03	4.218E+03	2.488E+03	3.046E+03	**1.206E+03**
	50	1.443E+04	1.493E+04	8.408E+03	9.020E+03	1.048E+04	9.582E+03	1.559E+04	1.002E+04	9.953E+03	1.487E+04	8.990E+03	1.156E+04	9.514E+03	1.606E+04	**5.507E+03**	8.953E+03	6.711E+03
	90	2.028E+04	2.551E+04	1.364E+04	1.433E+04	2.048E+04	1.453E+04	2.933E+04	1.661E+04	1.785E+04	2.892E+04	1.557E+04	2.058E+04	1.415E+04	3.001E+04	1.382E+04	**9.754E+03**	1.026E+04
C_{16}	10	8.828E-01	6.401E-03	3.999E-01	6.087E-01	1.690E-01	6.869E-03	1.287E+00	2.038E-01	2.855E-01	4.145E-03	9.783E-01	1.088E+00	9.322E-03	3.745E-02	4.581E-03	6.760E-01	**2.378E-03**
	30	2.517E+00	2.484E+00	1.544E+00	7.081E+00	2.832E-01	6.775E-03	3.051E+00	2.819E-01	3.163E-01	2.671E+00	1.242E+00	2.722E+00	9.348E-03	4.201E-02	5.817E-03	2.007E+00	**5.490E-03**
	50	3.914E+00	3.930E+00	3.422E+00	4.606E+00	1.594E+00	3.477E-02	4.502E+00	4.940E-01	1.269E+00	3.300E-02	1.415E+00	4.056E+00	5.168E-02	4.671E+00	**2.739E-02**	2.982E-02	3.098E+00
	90	4.083E+00	4.216E+00	2.296E+00	3.290E+00	1.895E-02	1.829E-02	5.027E+00	2.652E-01	1.524E+00	4.490E-01	9.731E-01	4.561E+00	3.117E-02	4.977E+00	**1.744E-02**	1.988E-02	3.908E+00
C_{17}	10	1.103E+03	3.847E+02	**9.927E+00**	1.237E+03	2.903E+01	5.985E-01	1.043E+01	4.964E+01	3.202E+01	1.365E+01	2.572E+01	3.313E+01	1.260E+01	3.483E+01	1.634E+01	1.300E+01	1.004E+01
	30	6.401E+01	7.041E+01	**3.528E+01**	6.854E+01	3.417E+01	3.531E+02	8.330E+02	6.125E+02	4.378E+02	7.615E+02	1.360E+02	2.191E+02	6.598E+01	4.301E+02	8.134E+01	6.115E+01	4.717E+01
	50	2.852E+02	2.576E+02	1.812E+02	6.343E+02	1.631E+03	1.008E+03	1.466E+03	1.052E+03	1.384E+03	**8.540E+01**	7.867E+02	8.303E+02	6.463E+02	1.637E+03	5.932E+02	6.679E+02	**1.278E+02**
	90	9.113E+02	6.990E+02	6.123E+02	1.913E+03	4.042E+03	2.303E+03	3.156E+03	2.461E+03	3.495E+03	3.749E+02	2.187E+03	2.246E+03	2.040E+03	4.867E+03	1.895E+03	1.373E+01	2.945E+01
C_{18}	10	2.672E+01	3.802E+02	2.504E+01	1.308E+01	2.959E+01	4.670E+01	3.617E+01	5.353E+01	2.903E+01	1.416E+01	3.283E+01	3.449E+01	**1.243E+01**	3.965E+01	1.669E+01	9.711E+01	**4.655E+01**
	30	2.481E+01	2.354E+02	1.298E+02	6.534E+01	3.022E+02	2.912E+02	8.706E+02	5.637E+02	4.874E+02	7.510E+02	1.986E+02	2.241E+02	5.971E+01	4.240E+02	7.641E+01	6.111E+01	2.125E+02
	50	5.897E+02	5.039E+02	4.124E+02	6.665E+02	1.795E+03	9.761E+02	1.466E+03	1.028E+03	1.308E+03	6.292E+02	8.437E+02	8.177E+02	6.684E+02	**9.242E+01**	5.929E+02	2.056E+02	3.579E+02
	90	1.365E+03	1.094E+03	9.356E+02	1.967E+03	3.996E+03	2.283E+03	3.126E+03	2.457E+03	3.233E+03	2.720E+03	2.257E+03	2.313E+03	2.016E+03	4.984E+03	**2.356E+02**	2.056E+03	3.579E+03
C_{19}	10	5.470E-01	3.427E+02	1.188E+02	1.329E+00	1.520E+01	1.266E+02	4.246E+00	3.148E+00	1.137E+00	1.282E+02	1.712E+00	1.837E+00	1.237E+00	2.179E+00	**3.418E-01**	7.046E-01	3.982E-01
	30	3.650E+00	7.378E+02	3.091E+00	6.897E+01	4.957E+01	9.020E+00	3.328E+05	5.334E+02	2.334E+01	2.790E+02	1.650E+01	1.725E+01	7.025E+00	5.095E+02	3.833E+00	5.419E+00	**2.643E+00**
	50	2.305E+01	2.708E+01	1.576E+01	1.080E+04	6.396E+05	2.680E+04	6.273E+05	1.294E+05	2.283E+04	1.759E+01	1.777E+04	7.379E+03	8.866E+03	1.897E+02	2.875E+02	1.871E+03	**7.039E+00**
	90	1.863E+03	9.806E+01	5.327E+01	2.416E+03	6.956E+06	3.266E+06	1.809E+06	9.081E+06	1.273E+06	7.762E+02	3.684E+05	2.856E+05	2.161E+05	1.178E+05	4.760E+04	1.075E+05	**3.195E+01**
C_{20}	10	2.834E+01	2.829E+02	2.943E+01	6.239E+01	6.251E+01	9.963E-01	3.526E+01	2.695E+01	4.377E+01	1.994E+01	2.345E+01	5.426E+01	9.270E+01	4.417E+01	1.242E+01	1.265E+01	**1.007E+01**
	30	3.993E+02	3.524E+02	**2.247E+02**	1.016E+03	7.689E+02	8.121E+02	6.341E+02	6.699E+02	8.313E+02	7.263E+02	9.249E+02	6.280E+02	4.774E+02	8.898E+02	8.220E+02	2.497E+02	2.488E+02
	50	3.893E+02	4.172E+02	**2.700E+02**	1.649E+03	5.060E+03	8.565E+02	1.002E+03	1.367E+03	1.252E+03	3.971E+02	1.699E+03	2.047E+03	1.501E+03	1.332E+03	1.347E+03	2.985E+02	2.928E+02
	90	9.107E+02	5.496E+02	8.252E+02	2.989E+03	1.017E+04	2.968E+03	4.356E+03	6.202E+03	3.437E+03	1.398E+03	5.142E+03	3.465E+03	1.591E+03	2.405E+03	4.802E+03	3.636E+03	**4.587E+02**

Bold font : Best value

Table 8 Comparative analysis of existing and new algorithms for mean fitness values over 30 runs on the CEC2013 benchmark functions ($C_{21} - C_{28}$) for considered dimensions

Fn.	D	MPSO	SDE	SBBO	GSA	OGSA	mDGSA	GGSA	PGSA	MGSA(I)	MGSA(II)	EGSA(I)	EGSA(II)	EGSA(III)	LKGSA	CKGSA	EKGSA	IGSA
C_{21}	10	3.668E+02	3.733E+02	3.582E+02	3.502E+02	3.802E+02	3.902E+02	3.802E+02	4.002E+02	3.865E+02	4.202E+02	3.902E+02	3.403E+02	3.802E+02	4.082E+02	3.702E+02	4.023E+02	**3.409E+02**
	30	3.119E+02	**2.546E+02**	2.936E+02	3.261E+02	6.519E+02	3.261E+02	2.525E+02	1.478E+02	3.079E+02	2.502E+03	3.260E+02	4.043E+02	3.079E+02	1.532E+03	3.079E+02	2.676E+02	2.676E+02
	50	6.895E+02	8.755E+02	8.947E+02	3.197E+03	4.480E+03	3.362E+03	4.587E+03	3.798E+03	3.126E+03	9.200E+02	3.335E+03	3.089E+03	3.179E+03	6.477E+03	2.553E+03	2.925E+03	**5.322E+02**
	90	9.012E+02	**3.924E+02**	6.892E+02	4.667E+03	1.038E+05	4.903E+03	6.891E+03	6.068E+03	6.280E+03	6.960E+02	4.699E+03	4.793E+03	4.714E+03	1.342E+03	4.077E+03	4.474E+03	5.453E+02
C_{22}	10	1.829E+02	1.825E+02	4.322E+02	1.753E+02	2.032E+02	2.603E+02	5.015E+01	2.317E+02	9.732E+02	2.730E+02	1.726E+02	1.711E+02	1.687E+02	2.026E+02	1.798E+02	3.026E+02	**1.139E+01**
	30	**9.156E+02**	2.284E+02	1.633E+03	6.399E+02	6.971E+02	7.731E+03	8.187E+02	7.387E+03	3.677E+03	8.941E+03	6.203E+03	7.119E+03	6.367E+03	5.980E+03	6.052E+03	2.030E+03	1.608E+03
	50	4.108E+03	7.429E+03	5.006E+03	1.300E+04	1.477E+04	1.403E+04	1.637E+04	1.376E+04	9.759E+03	7.234E+03	1.317E+04	1.456E+04	1.295E+04	1.705E+04	**1.033E+03**	1.301E+04	3.906E+03
	90	1.369E+04	2.069E+04	1.328E+04	2.481E+04	2.832E+04	2.481E+04	3.041E+04	2.621E+04	2.268E+04	1.842E+04	2.522E+04	2.826E+04	2.409E+04	3.247E+04	2.404E+04	**4.824E+03**	5.093E+03
C_{23}	10	7.372E+02	1.754E+02	1.312E+03	1.194E+03	1.761E+03	2.026E+03	1.138E+03	1.982E+03	8.890E+02	**3.565E+02**	1.208E+03	1.276E+03	1.195E+03	1.679E+03	1.296E+03	6.712E+02	1.108E+03
	30	6.856E+03	7.835E+03	5.325E+03	5.757E+03	6.477E+03	6.319E+03	8.209E+03	7.010E+03	6.189E+03	9.019E+03	5.905E+03	6.579E+03	5.842E+03	6.702E+03	5.698E+03	3.422E+03	**2.607E+03**
	50	1.476E+04	1.523E+04	1.120E+04	1.223E+04	1.372E+04	1.270E+04	1.739E+04	1.383E+04	1.318E+04	8.858E+03	1.291E+04	1.406E+04	1.247E+04	1.729E+04	1.238E+04	1.246E+04	**6.342E+03**
	90	2.287E+04	2.652E+04	1.813E+04	2.339E+04	2.718E+04	2.316E+04	3.167E+04	2.549E+04	2.327E+04	1.656E+04	2.353E+04	2.704E+04	2.294E+04	3.211E+04	2.237E+04	2.271E+04	**1.327E+04**
C_{24}	10	2.083E+02	2.463E+02	2.168E+02	2.221E+02	**1.850E+02**	2.554E+02	2.130E+02	2.537E+02	2.147E+02	2.000E+02	2.235E+02	2.208E+02	2.153E+02	2.337E+02	2.225E+02	2.045E+02	1.918E+02
	30	2.715E+02	2.863E+02	2.626E+02	3.133E+02	4.677E+02	5.590E+02	6.168E+02	5.211E+02	3.277E+02	4.077E+02	3.476E+02	3.006E+02	3.464E+02	3.945E+02	3.496E+02	2.434E+02	**2.003E+02**
	50	3.480E+02	3.831E+02	3.050E+02	9.681E+02	2.226E+02	1.275E+03	1.127E+03	1.095E+03	4.514E+02	3.681E+02	8.050E+02	5.447E+02	9.312E+02	**2.497E+02**	8.203E+02	9.297E+02	2.909E+02
	90	4.438E+02	5.169E+02	3.900E+02	2.561E+03	4.064E+03	2.730E+03	3.047E+03	2.782E+03	1.055E+03	3.579E+03	2.580E+03	2.410E+03	2.513E+03	2.937E+03	2.318E+03	2.360E+03	**3.530E+02**
C_{25}	10	2.096E+02	2.386E+02	2.138E+02	2.108E+02	2.119E+02	2.451E+02	2.094E+02	2.450E+02	2.161E+02	1.997E+02	2.075E+02	2.084E+02	2.083E+02	2.298E+02	2.126E+02	2.030E+02	**1.787E+02**
	30	2.843E+02	2.930E+02	2.997E+02	3.867E+02	3.946E+02	4.325E+02	4.259E+02	4.364E+02	3.529E+02	4.111E+02	3.932E+02	3.854E+02	3.875E+02	4.044E+02	3.986E+02	2.568E+02	**2.000E+02**
	50	3.992E+02	3.991E+02	3.883E+02	6.665E+02	7.730E+02	6.956E+02	6.498E+02	6.758E+02	5.322E+02	3.383E+02	6.674E+02	6.299E+02	6.724E+02	6.805E+02	6.464E+02	6.658E+02	**3.204E+02**
	90	5.460E+02	5.499E+02	5.422E+02	1.233E+03	1.612E+03	1.274E+04	8.908E+02	1.303E+03	9.172E+02	5.376E+02	1.266E+03	1.274E+03	1.293E+03	1.336E+03	1.188E+03	**1.219E+02**	4.151E+02
C_{26}	10	2.201E+02	3.052E+02	1.845E+02	3.285E+02	3.978E+02	3.257E+02	1.876E+02	3.113E+02	1.926E+02	1.886E+02	2.572E+02	2.185E+02	2.774E+02	2.524E+02	3.016E+02	1.677E+02	**1.437E+02**
	30	3.150E+02	2.113E+02	2.865E+02	3.414E+02	3.910E+02	3.983E+02	4.675E+02	4.329E+02	3.537E+02	2.939E+02	3.568E+02	3.164E+02	3.567E+02	3.915E+02	3.843E+02	**2.000E+02**	2.771E+02
	50	4.214E+02	3.128E+02	4.136E+02	4.636E+02	1.797E+03	5.616E+02	6.437E+02	6.093E+02	4.538E+02	**3.085E+02**	4.742E+02	4.119E+02	3.813E+02	5.574E+02	3.663E+02	3.980E+02	3.183E+02
	90	5.094E+02	6.287E+02	4.768E+02	1.188E+03	1.284E+05	1.808E+03	2.906E+03	2.477E+03	6.645E+02	**4.370E+02**	1.534E+03	8.053E+02	8.965E+02	2.728E+03	1.424E+03	1.153E+03	4.393E+03
C_{27}	10	3.848E+02	7.951E+02	4.915E+02	4.100E+02	3.257E+02	3.400E+02	4.247E+02	4.100E+02	5.226E+02	3.924E+02	4.014E+02	4.233E+02	4.250E+02	5.193E+02	3.922E+02	**3.167E+02**	3.465E+02
	30	6.891E+02	9.746E+02	1.094E+03	1.023E+03	9.571E+02	9.216E+02	8.220E+02	8.915E+02	7.207E+02	9.809E+02	1.051E+03	1.095E+03	8.975E+02	9.884E+02	9.204E+02	8.526E+02	**3.005E+02**
	50	1.672E+03	2.156E+03	1.543E+03	2.619E+03	5.349E+03	3.387E+03	3.626E+03	3.414E+03	2.379E+03	1.662E+03	2.723E+03	2.506E+03	2.758E+03	3.227E+03	2.496E+03	2.602E+03	**8.912E+02**
	90	2.655E+03	3.603E+03	2.193E+03	6.401E+03	1.075E+04	8.647E+03	1.007E+04	9.147E+03	4.823E+03	4.599E+03	5.480E+03	5.356E+03	6.531E+03	9.618E+03	5.381E+03	**1.330E+03**	1.779E+03
C_{28}	10	2.977E+02	2.086E+02	3.908E+02	6.036E+02	5.944E+02	9.618E+02	2.900E+02	9.435E+02	3.955E+02	2.920E+02	4.970E+02	6.037E+02	6.231E+02	8.279E+02	7.118E+02	2.900E+02	**1.929E+02**
	30	2.900E+02	3.200E+02	8.974E+02	4.031E+02	5.305E+03	5.086E+03	7.347E+03	4.944E+03	2.968E+03	6.072E+03	4.178E+03	4.254E+03	4.143E+03	3.981E+03	4.363E+03	2.900E+02	**2.218E+02**
	50	1.363E+03	4.592E+02	**4.246E+02**	8.542E+03	4.260E+04	9.100E+03	1.251E+04	9.667E+03	6.137E+03	4.363E+03	8.799E+03	9.258E+03	8.727E+03	1.143E+04	8.027E+03	8.436E+03	6.753E+03
	90	2.189E+03	1.377E+03	1.220E+03	1.282E+04	2.531E+04	1.343E+04	1.902E+04	1.623E+04	1.480E+04	3.794E+03	1.298E+04	1.471E+04	1.299E+04	2.220E+04	1.232E+04	1.283E+04	**3.933E+02**

Bold font : Best value

Table 9 Friedman test based on mean fitness values over 30 runs on the common benchmark functions ($F_1 - F_{17}$) for different dimensions

Rank	10 dims. Algorithm		30 dims. Algorithm		50 dims. Algorithm		90 dims. Algorithm	
1	IGSA	4.159	IGSA	4.955	IGSA	6.091	IGSA	5.818
2	GGSA	5.727	GGSA	6.114	mDGSA	6.318	MGSA(I)	6.000
3	MPSO	6.523	SDE	6.545	EKGSA	6.591	EKGSA	6.091
4	EGSA(III)	7.500	mDGSA	6.818	CKGSA	6.795	CKGSA	6.795
5	mDGSA	7.591	CKGSA	7.000	MGSA(I)	6.955	mDGSA	7.136
6	EKGSA	7.682	EGSA(I)	7.364	GSA	7.545	OGSA	7.568
7	CKGSA	7.705	GSA	7.841	OGSA	8.136	GSA	8.182
8	EGSA(II)	7.841	EGSA(II)	8.136	GGSA	8.250	EGSA(I)	8.273
9	GSA	8.159	MPSO	8.364	SDE	8.273	GGSA	8.364
10	LKGSA	9.455	CGSA	8.500	MPSO	8.591	EGSA(III)	8.614
11	EGSA(I)	9.523	MGSA(I)	8.682	EGSA(I)	9.045	MPSO	9.045
12	CGSA	9.591	LKGSA	9.841	EGSA(III)	9.955	SDE	9.773
13	MGSA(I)	10.068	EKGSA	10.091	SBBO	10.409	SBBO	9.773
14	SDE	11.545	OGSA	11.659	LKGSA	11.432	LKGSA	11.909
15	OGSA	11.795	SBBO	12.091	EGSA(II)	11.932	EGSA(II)	12.477
16	SBBO	12.091	EGSA(III)	13.909	CGSA	13.182	CGSA	13.364
17	PGSA	16.045	PGSA	15.091	PGSA	13.500	PGSA	13.818

Table 10 Friedman test based on mean fitness values over 30 runs on the CEC benchmark functions ($C_1 - C_{28}$) for different dimensions

Rank	10 dims. Algorithm		30 dims. Algorithm		50 dims. Algorithm		90 dims. Algorithm	
1	IGSA	4.214	IGSA	3.143	IGSA	2.000	IGSA	2.071
2	mDGSA	5.000	EKGSA	3.679	SBBO	3.964	SBBO	3.357
3	MPSO	5.643	CGSA	5.071	CGSA	4.500	MPSO	5.143
4	EKGSA	5.679	SBBO	5.821	mDGSA	5.393	mDGSA	5.179
5	CGSA	7.214	MPSO	6.321	MPSO	5.750	CGSA	5.571
6	GGSA	7.750	SDE	6.875	SDE	6.893	SDE	6.571
7	SBBO	8.214	GGSA	7.232	CKGSA	7.000	CKGSA	6.964
8	EGSA(I)	8.250	CKGSA	7.696	EKGSA	7.357	EKGSA	7.250
9	CKGSA	8.429	GSA	8.000	GGSA	9.536	GGSA	9.464
10	EGSA(II)	8.464	EGSA(II)	9.464	EGSA(II)	9.714	GSA	9.571
11	GSA	8.929	EGSA(III)	10.143	GSA	9.821	EGSA(II)	10.214
12	LKGSA	10.464	MGSA(I)	10.821	EGSA(III)	10.750	MGSA(I)	11.214
13	EGSA(III)	11.893	LKGSA	12.000	MGSA(I)	12.536	EGSA(III)	11.464
14	OGSA	12.321	OGSA	12.232	PGSA	13.429	PGSA	12.929
15	SDE	12.964	PGSA	14.179	LKGSA	13.536	EGSA(I)	14.964
16	MGSA(I)	13.464	mDGSA	14.321	EGSA(I)	15.357	LKGSA	15.321
17	PGSA	14.107	EGSA(I)	16.000	OGSA	15.464	OGSA	15.750

Table 6 (continued)

Fn.	D	MPSO	SDE	SBBO	GSA	mDGSA	OGSA	GGSA	PGSA	MGSA(I)	MGSA(II)	EGSA(I)	EGSA(II)	EGSA(III)	LKGSA	CKGSA	EKGSA	IGSA
C_9	10	2.995E+00	1.006E+01	6.045E+00	3.393E+00	9.247E+00	5.462E+00	3.953E+00	9.445E+00	4.394E+00	1.277E+00	4.153E+00	4.749E+00	3.094E+00	**1.235E+00**	4.521E+00	2.244E+00	5.326E+00
	30	2.329E+01	3.664E+01	2.702E+01	3.180E+01	3.894E+01	3.357E+01	4.549E+01	4.555E+01	3.394E+01	4.320E+01	3.474E+01	3.524E+01	3.073E+01	3.670E+01	3.043E+01	1.770E+01	**7.025E+00**
	50	5.366E+01	7.458E+01	5.396E+01	5.875E+01	7.011E+01	7.380E+01	8.044E+01	7.667E+01	6.768E+01	**2.560E+01**	6.194E+01	6.561E+01	6.126E+01	7.626E+01	6.122E+01	5.818E+01	3.470E+01
	90	8.534E+01	1.323E+02	7.927E+01	1.299E+02	1.383E+02	1.520E+02	1.579E+02	1.530E+02	1.262E+02	**5.238E+01**	1.367E+02	1.386E+02	1.290E+02	1.571E+02	1.272E+02	1.270E+02	5.288E+01
C_{10}	10	4.863E-01	7.775E-02	1.431E+00	3.817E-01	2.175E-01	8.453E-02	2.281E+00	4.927E-01	3.500E-01	2.030E-03	1.135E+00	1.363E+00	4.833E-03	6.736E-02	1.642E-03	6.408E-02	**7.620E-04**
	30	7.972E-01	3.548E+01	2.016E+00	9.297E+01	2.127E-02	5.462E+01	9.037E+03	8.459E+02	1.604E+03	5.505E+03	6.161E+00	6.020E+00	1.118E-01	1.455E+03	**4.704E-03**	4.617E-02	1.255E-02
	50	1.548E+02	1.598E+03	1.811E+01	1.548E+03	3.437E+03	1.146E+04	1.449E+04	6.251E+03	5.076E+03	3.419E+01	1.931E+03	1.499E+03	1.339E+03	1.199E+04	7.273E+02	1.066E+03	**2.218E-01**
	90	2.880E+02	1.273E+03	4.547E+01	9.661E+03	1.425E+04	3.270E+04	3.096E+04	2.054E+04	1.486E+04	4.381E+02	1.127E+02	9.888E+03	9.913E+03	3.147E+04	5.191E+03	7.737E+03	**8.643E-02**

Bold font : Best value

and the alternative hypothesis signifies that all samples are significantly different. In the tables, p-value is less than the considered significance level, i.e. $\alpha = 0.05$ which indicates that the null hypothesis (H0) is rejected. Moreover, IGSA attained minimum mean rank value among the comparative algorithms in all tables. Therefore, it is perceptible that there is a significant difference between IGSA and other algorithms for both sets over 10, 30, 50, and 90 dimensions.

Further, box-plots have been drawn to analyze the consistency of the new variant for different dimensions in terms of the average failure rate. Failure rate corresponds to the number of runs in which an algorithm fails to achieve the optimum value. To count the same, the considered algorithms have been executed 30 times where each execution consists of 30 runs. Figure 8 illustrates the box-plots over different dimensions i.e. 10, 30, 50, and 90. The considered algorithms are depicted on the horizontal axis, while the average failure rate is denoted on the vertical axis. In the figures, IGSA is comparatively more consistent with small interquartile range and medians. Therefore, it is pertinent from experiments that IGSA attains better global and local search balance along with high precision.

5.2 Experimental analysis of the proposed clustering method

The experimental analysis of the proposed clustering (KIGSA-C) method for CoVID19 diagnosis is evaluated on three types of chest images, namely X-ray, CT-scan, and Ultrasound. Table 11 tabulates the considered datasets for the three types of chest images. In the X-ray dataset, there are 234 chest images of CoVID19 patients that are publicly available on [84]. A similar count of non-CoVID19 images is considered from a publicly available dataset which consists of chest X-ray of patients who are infected from other viral and bacterial pneumonia like, MERS, SARS, and ARDS [85]. Further, four CNN models namely, DenseNet-161, ResNet-34, VGG-16, and MobileNet-V2 are considered to perform feature extraction as they have top-5 error value as less than 10 [70]. For feature extraction, the last layer of these pre-trained models is truncated and the remaining combination of layers, i.e. convolutional, non-linear activation, pooling, and fully-connected, are used to extract features. Table 12 tabulates the considered CNN models for TLFE along with the number of extracted features. After extracting the deep features, optimal cluster centroids are obtained through the KIGSA-C method which is used to label the considered images in two categories, namely CoVID19 and non-CoVID19. As labeled dataset is used for experimentation, the performance of the proposed method can be evaluated on different classification parameters, such as accuracy, precision, and F1-score, by comparing the predicted label

Fig. 8 Boxplot of IGSA and other considered algorithms for different dimensions
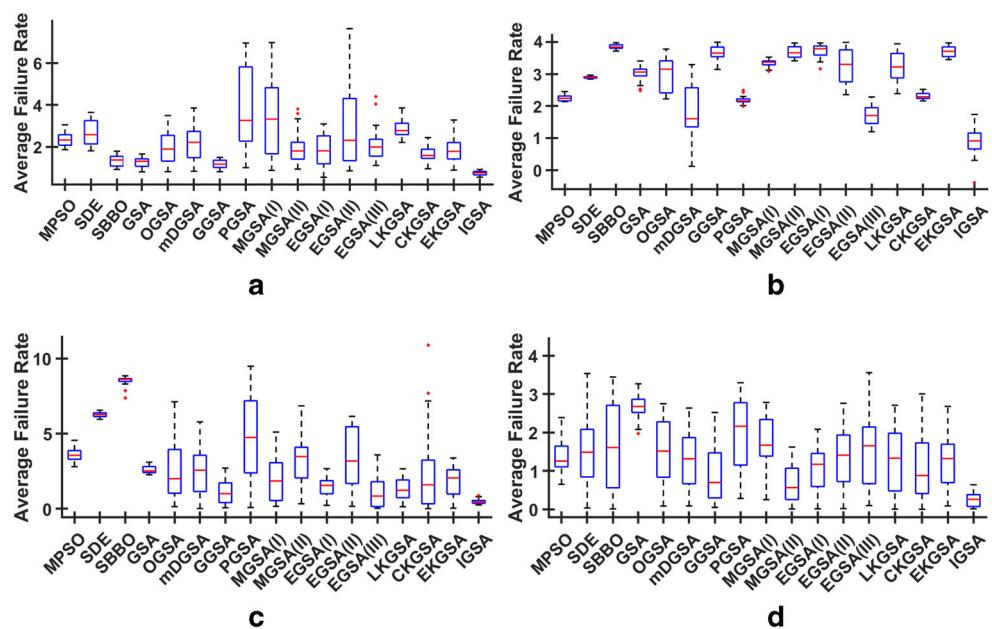
with actual label [42]. Moreover, the results of the proposed KIGSA-C method is compared against two methods, i.e. Kmeans and Kmeans-based gravitational search algorithm clustering (KGSA-C). Table 13 tabulates the confusion matrices between CoVID19 and non-CoVID19 classes for the considered methods over different TLFE models. Bold entries present the best values. From Table 13, it is observable that the proposed method identifies more than 98.5% of the CoVID19 images correctly. Moreover, the false-positive rate of the proposed method is comparatively low than the other methods. In terms of false-negative, the KIGSA-C method attained competitive results. For better visualization comparison, the classification accuracy of the considered methods on the X-ray dataset is plotted as bar-chart in Fig. 9. In the figure, $X-axis$ denotes the names of the method while $Y-axis$ represents the obtained accuracy. From the figures, it can be claimed that the proposed KIGSA-C method outperforms other considered methods with a margin of more than 1% approximately. Further, the performance of the proposed method is evaluated on four more parameters, namely sensitivity, specificity, precision, and F1-score. The formulation of each parameter

is expressed in (15) – (18) respectively [88]. Table 14 presents the results of the considered methods on the studied parameters for X-ray images. The bold represents the best value. It can be observed for the table that the proposed method has consistency in the results.

$$Sensitivity = \frac{true\ positives}{true\ positives + false\ negatives} \quad (15)$$

$$Specificity = \frac{true\ negatives}{true\ negatives + false\ positives} \quad (16)$$

$$Precision = \frac{true\ positives}{true\ positives + false\ positives} \quad (17)$$

$$F_1\ score = 2 \star \frac{precision \star recall}{precision + recall} \quad (18)$$

Further, the performance of the considered methods is examined on CT-scan and Ultrasound images. The CT-scan dataset referred from a publicly available resource [86]. This dataset consists of 392 CT-scan images of CoVID19 patients with an equal number of non-CoVID19

Table 11 Considered CoVID19 datasets

Type of chest image	Ref.
X-ray	[84, 85]
CT-scan	[86]
Ultrasound	[87]

Table 12 Details of the considered TLFE models taken from [70]

Model	Top-5 error	Number of extracted features
DenseNet-161	6.2	2208
ResNet-34	8.58	512
VGG-16	9.62	512
MobileNet V2	9.71	1280

Table 13 Confusion matrix for X-ray images

Classes	DenseNet-161 CoVID19	non- CoVID19	ResNet-34 CoVID19	non- CoVID19	VGG-16 CoVID19	non- CoVID19	MobileNet-V2 CoVID19	non- CoVID19	Method
CoVID19	0.9787	0.0213	0.9702	0.0298	0.9660	0.0340	0.9830	0.0170	Kmeans
	0.9830	0.0170	0.9872	0.0128	0.9702	0.0298	0.9915	0.0085	KGSA-C
	0.9872	0.0128	**0.9915**	0.0085	**0.9872**	0.0128	**0.9957**	0.0043	KIGSA-C
	0.1021	0.8979	0.0383	0.9617	0.0511	0.9489	0.0255	0.9745	Kmeans
non-	0.0936	0.9064	0.0255	0.9745	0.0383	0.9617	0.0213	**0.9787**	KGSA-C
CoVID19	0.0766	**0.9234**	0.0213	**0.9830**	0.0340	**0.9660**	0.0213	**0.9787**	KIGSA-C

Fig. 9 Classification accuracy of considered methods on X-ray dataset
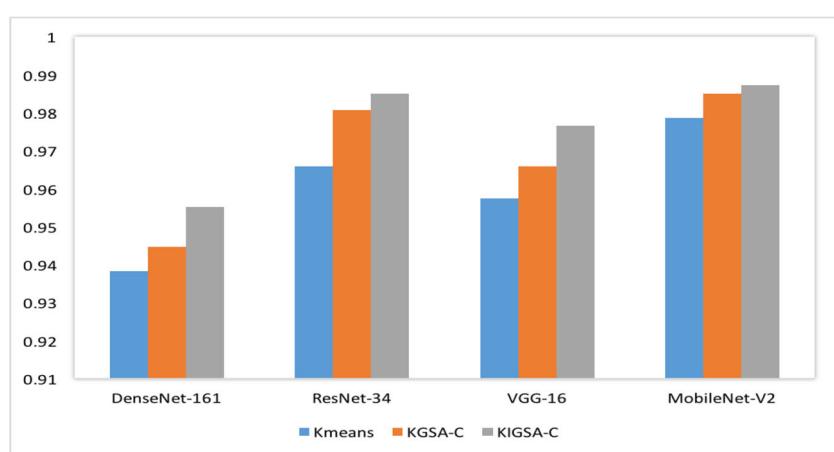
Table 14 Performance of considered methods on classification parameters for Xray images

Model	Parameters	Kmeans	KGSA-C	KIGSA-C
DenseNet-161	Sensitivity	0.9055	0.9130	**0.9280**
	Specificity	0.9769	0.9816	**0.9864**
	Precision	0.9787	0.9830	**0.9872**
	F1-score	0.9407	0.9467	**0.9567**
ResNet-34	Sensitivity	0.9620	0.9748	**0.9790**
	Specificity	0.9700	0.9871	**0.9914**
	Precision	0.9702	0.9872	**0.9915**
	F1-score	0.9661	0.9810	**0.9852**
VGG-16	Sensitivity	0.9498	0.9620	**0.9667**
	Specificity	0.9654	0.9700	**0.9870**
	Precision	0.9660	0.9702	**0.9872**
	F1-score	0.9578	0.9661	**0.9768**
MobileNet-V2	Sensitivity	0.9747	0.9790	**0.9791**
	Specificity	0.9828	0.9914	**0.9957**
	Precision	0.9830	0.9915	**0.9957**
	F1-score	0.9788	0.9852	**0.9873**

Table 15 Performance comparison of considered methods on CT-scan and Ultrasound dataset

Dataset	Methods	Sensitivity	Specificity	Precision	F1-score	Accuracy
CT-scans	Kmeans	0.6385	0.6077	0.5587	0.5959	0.6212
	KGSA-C	0.6561	0.6233	0.5791	0.6152	0.6378
	KIGSA-C	**0.6628**	**0.6293**	**0.5867**	**0.6225**	**0.6441**
Ultrasound	Kmeans	0.9751	**1.0000**	**1.0000**	0.9874	0.9872
	KGSA-C	0.9792	**1.0000**	**1.0000**	0.9895	0.9894
	KIGSA-C	**0.9874**	**1.0000**	**1.0000**	**0.9937**	**0.9936**

CT-scans. For the Ultrasound dataset, the publicly available images from [87] are considered. It is a relatively small dataset that consists of 19 images in the CoVID19 category and 14 images in the non-CoVID19 category. Further, MobileNet-V2 is employed for feature extraction as considered methods have reported comparatively better results on it in Table 13. Table 15 depicts the performance of considered methods in terms of sensitivity, specificity, precision, F1-score, and accuracy. Here, bold value depicts the best value. It is interesting to note that the results of the proposed method on CT-scan images are quite promising in comparison to other methods, despite there is high similarity between CT-scan images of CoVID19 and non-CoVID19 [see Figs. 1b and 2b]. On the Ultrasound dataset, the specificity and precision of all the methods are 1. Moreover, the proposed method attained the highest accuracy, i.e. 99.3%. Thus, it is pertinent from experiments that KIGSA-C is efficient among all considered methods and may be used as an alternative tool to diagnose CoVID19 from medical images.

6 Conclusion

In this paper, a new clustering method, Kmeans-based gravitational search algorithm clustering (KIGSA-C) method, has been introduced for the diagnosis of CoVID19 from the medical images. Although many supervised models exist in the literature, the generalization of these models may suffer due to the limited availability of datasets. To remedy the same, a new clustering is presented. In the proposed method, features are extracted from the considered images through a deep learning model. The extracted features are further optimally clustered through a novel variant, improved gravitational search algorithm (IGSA). The obtained optimal cluster centroids are then used to perform the labeling of the considered images into CoVID19 and non-CoVID19. Further, the proposed variant, IGSA, has been validated against 16 recent metaheuristic algorithms over two sets of benchmark functions belonging to the three types of problems, namely unimodal, multimodal,

and real parameters single-objective optimization problems of IEEE Congress on Evolutionary Computation (CEC), 2013. The experimental performance has been evaluated over four different functional dimensions, i.e. 10, 30, 50, and 90 and studied in terms of mean fitness value, Friedman test, and boxplot. It has been observed from experimental results that IGSA has surpassed the considered algorithms over the maximum number of benchmark problems in each dimension. Moreover, the Friedman test has statistically ranked the IGSA as the top algorithm among the considered algorithms. The analysis of the box-plots indicates that the searching behavior of IGSA is better with consistency. Thus, it can be concluded that IGSA achieves better precision with a balanced trade-off between exploration and exploitation. Further, the performance of the new KIGSA-C method has been evaluated against Kmeans and Kmeans-based gravitational search algorithm clustering methods on three types of medical chest images, namely X-ray, CT-scans, and Ultrasound images. In experiments, the feature extraction is performed through four pre-trained deep learning models, namely DenseNet-161, ResNet-34, VGG-16, and MobileNet-V2. The experimental results are measured in terms of sensitivity, specificity, precision, F1-score, and accuracy. Experiments affirm that the proposed KIGSA-C method is efficient and can be used as an alternative tool in aiding the diagnosis of CoVID-19.

In the future, real-time datasets may be explored to enhance the efficiency of the proposed model. Moreover, it may be scaled upon a distributed framework to reduce the computation time. Additionally, a parallel version of the proposed method can be explored to handle big datasets by employing architectures like spark or Hadoop.

References

1. Organization WH (2020) Novel coronavirus (2019-ncov): situation report, 11, Technical documents (2020-01-31)
2. 20200219-sitrep-30-covid-19.pdf. https://www.who.int/docs/default-source/coronavirus/situation-reports/20200219-sitrep-30-covid-19.pdf. Accessed 27 May 2020

3. Shereen MA, Khan S, Kazmi A, Bashir N, Siddique R (2020) Covid-19 infection: origin, transmission, and characteristics of human coronaviruses. Journal of Advanced Research

4. Kassani SH, Kassasni PH, Wesolowski MJ, Schneider KA, Deters R (2020) Automatic detection of coronavirus disease (covid-19) in x-ray and ct images: a machine learning-based approach. arXiv:2004.10641

5. Rothan HA, Byrareddy SN (2020) The epidemiology and pathogenesis of coronavirus disease (covid-19) outbreak. Journal of Autoimmunity: pp 1–4

6. Coronavirus (covid-19) - google news. https://news.google.com/covid19/map?hl=en-IN&gl=IN&ceid=IN:en. Accessed on 01 June 2020

7. Ai T, Yang Z, Hou H, Zhan C, Chen C, Lv W, Tao Q, Sun Z, Xia L (2020) Correlation of chest ct and rt-pcr testing in coronavirus disease 2019 (covid-19) in China: a report of 1014 cases. Radiology: 296(2):E32–E40

8. Singh D, Kumar V, Kaur M (2020) Classification of covid-19 patients from chest ct images using multi-objective differential evolution–based convolutional neural networks. European Journal of Clinical Microbiology & Infectious Diseases: 1–11

9. Wang D, Hu B, Hu C, Zhu F, Liu X, Zhang J, Wang B, Xiang H, Cheng Z, Xiong Y, et al. (2020) Clinical characteristics of 138 hospitalized patients with 2019 novel coronavirus–infected pneumonia in Wuhan, China. Jama 323(11):1061–1069

10. Wang Y, Dong C, Hu Y, Li C, Ren Q, Zhang X, Shi H, Zhou M (2020) Temporal changes of ct findings in 90 patients with covid-19 pneumonia: a longitudinal study. Radiology: 296(2):E55–E64

11. Fang Y, Zhang H, Xu Y, Xie J, Pang P, Ji W (2020) Ct manifestations of two cases of 2019 novel coronavirus (2019-ncov) pneumonia. Radiology 295(1):208–209

12. Xie X, Zhong Z, Zhao W, Zheng C, Wang F, Liu J (2020) Chest ct for typical 2019-ncov pneumonia: relationship to negative rt-pcr testing. Radiology: 296(2):E41–E45

13. Narin A, Kaya C, Pamuk Z (2020) Automatic detection of coronavirus disease (covid-19) using x-ray images and deep convolutional neural networks. arXiv:2003.10849

14. Agarwal T, Mittal H (2019) Performance comparison of deep neural networks on image datasets. In: 2019 twelfth international conference on contemporary computing (IC3). IEEE, pp 1–6

15. Pandey AC, Garg M, Rajput S (2019) Enhancing text mining using deep learning models. In: Proc. of twelfth IEEE international conference on contemporary computing (IC3). IEEE, pp 1–5

16. Pandey AC, Rajpoot DS, Saraswat M (2020) Feature selection method based on hybrid data transformation and binary binomial cuckoo search. Journal of Ambient Intelligence and Humanized Computing 11(2):719–738

17. Tripathi AK, Sharma K, Bala M (2018) A novel clustering method using enhanced grey wolf optimizer and mapreduce. Big Data Research 14:93–100

18. Mittal H, Saraswat M (2020) A new fuzzy cluster validity index for hyper-ellipsoid or hyper-spherical shape close clusters with distant centroids. IEEE Transactions on Fuzzy Systems

19. Pandey AC, Rajpoot DS, Saraswat M (2017) Twitter sentiment analysis using hybrid cuckoo search method. Information Processing & Management 53:764–779

20. Pal R, Saraswat M (2019) Grey relational analysis based keypoints selection in bag-of-features for histopathological image classification. Recent Patents on Computer Science 12(4):260–268

21. Tripathi AK, Sharma K, Bala M, Kumar A, Menon VG, Bashir AK (2020) A parallel military dog based algorithm for clustering big data in cognitive industrial internet of things. IEEE Transactions on Industrial Informatics

22. Tripathi AK, Mittal H, Saxena P, Gupta S (2020) A new recommendation system using map-reduce-based tournament empowered whale optimization algorithm. Complex & Intelligent Systems: 1–13

23. Ashish T, Kapil S, Manju B (2018) Parallel bat algorithm-based clustering using mapreduce. In: Networking communication and data knowledge engineering. Springer

24. Mittal H, Saraswat M (2019) Classification of histopathological images through bag-of-visual-words and gravitational search algorithm. In: Soft computing for problem solving. Springer

25. Tripathi AK, Sharma K, Bala M (2018) Dynamic frequency based parallel k-bat algorithm for massive data clustering (dfbpkba). International Journal of System Assurance Engineering and Management 9:866–874

26. Gupta V, Singh A, Sharma K, Mittal H (2018) A novel differential evolution test case optimisation (detco) technique for branch coverage fault detection. In: Smart computing and informatics. Springer

27. Dixit M, Upadhyay N, Silakari S (2015) An exhaustive survey on nature inspired optimization algorithms. Int J Software Eng Applic 9:91–104

28. Pal R, Yadav S, Karnwal R, et al. (2020) Eewc: energy-efficient weighted clustering method based on genetic algorithm for hwsns. Complex & Intelligent Systems: 1–10

29. Whitley D (1994) A genetic algorithm tutorial. Statistics and Computing 4:65–85

30. Storn R, Price K (1997) Differential evolution–a simple and efficient heuristic for global optimization over continuous spaces. J Glob Optim 11:341–359

31. Kennedy J, Eberhart R (1995) Particle swarm optimization. In: IEEE internation conference on neural networks

32. Dorigo M, Birattari M, Stützle T (2006) Ant colony optimization. IEEE Comput Intell Mag 1:28–39

33. Simon D (2008) Biogeography-based optimization. IEEE Trans Evol Comput 12:702–713

34. Jadon SS, Bansal JC, Tiwari R, Sharma H (2014) Artificial bee colony algorithm with global and local neighborhoods. International Journal of System Assurance Engineering and Management 9:1–13

35. Mohammed AS, Shukla V, Pandey AC (2020) Enhancing sentiment analysis using enhanced whale optimisation algorithm. International Journal of Intelligent Information and Database Systems 13(2-4):208–230

36. Rashedi E, Nezamabadi-Pour H, Saryazdi S (2009) Gsa: a gravitational search algorithm. Inf Sci 179:2232–2248

37. Rashedi E, Rashedi E, Nezamabadi-pour H (2018) A comprehensive survey on gravitational search algorithm. Swarm and Evolutionary Computation 41:141–158

38. Mittal H, Tripathi A, Pandey AC, Pal R (2020) Gravitational search algorithm: a comprehensive analysis of recent variants. Multimedia Tools and Applications: 1–28

39. Mittal H, Saraswat M (2018) ckgsa based fuzzy clustering method for image segmentation of rgb-d images. In: Proc. of IEEE international conference on contemporary computing, India

40. Olivas F, Valdez F, Melin P, Sombra A, Castillo O (2019) Interval type-2 fuzzy logic for dynamic parameter adaptation in a modified gravitational search algorithm. Inf Sci 476:159–175

41. Mittal H, Saraswat M, Pal R (2020) Histopathological image classification by optimized neural network using igsa. In: International conference on distributed computing and internet technology. Springer, pp 429–436

42. Pandey AC, Pal R, Kulhari A (2018) Unsupervised data classification using improved biogeography based optimization. International Journal of System Assurance Engineering and Management 9:821–829

43. Xu X, Jiang X, Ma C, Du P, Li X, Lv S, Yu L, Chen Y, Su J, Lang G (2002) Deep learning system to screen coronavirus disease 2019 pneumonia, 6(10): 1122–1129

44. Wang S, Kang B, Ma J, Zeng X, Xiao M, Guo J, Cai M, Yang J, Li Y, Meng X, et al. (2020) A deep learning algorithm using ct images to screen for corona virus disease (covid-19). MedRxiv

45. Hemdan EE-D, Shouman MA, Karar ME (2020) Covidx-net: a framework of deep learning classifiers to diagnose covid-19 in x-ray images. arXiv:2003.11055

46. Sethy PK, Behera SK (2020) Detection of coronavirus disease (covid-19) based on deep features. Preprints 2020030300. 2020

47. Wang L, Wong A (2020) Covid-net: a tailored deep convolutional neural network design for detection of covid-19 cases from chest radiography images. arXiv:2003.09871

48. Farooq M, Hafeez A (2020) Covid-resnet: a deep learning framework for screening of covid19 from radiographs. arXiv:2003.14395

49. Maghdid HS, Asaad AT, Ghafoor KZ, Sadiq AS, Khan MK (2020) Diagnosing covid-19 pneumonia from x-ray and ct images using deep learning and transfer learning algorithms. arXiv:2004.00038

50. Shaw B, Mukherjee V, Ghoshal S (2012) A novel opposition-based gravitational search algorithm for combined economic and emission dispatch problems of power systems. International Journal of Electrical Power & Energy Systems 35:21–33

51. Chatterjee A, Ghoshal S, Mukherjee V (2012) A maiden application of gravitational search algorithm with wavelet mutation for the solution of economic load dispatch problems. International Journal of Bio-Inspired Computation 4:33–46

52. Mirjalili S, Hashim SZM (2010) A new hybrid psogsa algorithm for function optimization. In: Proc. of IEEE international conference on computer and information application, China, pp 374–377

53. Sarafrazi S, Nezamabadi-Pour H, Saryazdi S (2011) Disruption: a new operator in gravitational search algorithm. Scientia Iranica 18:539–548

54. Niknam T, Golestaneh F, Malekpour A (2012) Probabilistic energy and operation management of a microgrid containing wind/photovoltaic/fuel cell generation and energy storage devices based on point estimate method and self-adaptive gravitational search algorithm. Energy 43:427–437

55. Li C, Zhou J, Xiao J, Xiao H (2012) Parameters identification of chaotic system by chaotic gravitational search algorithm, Chaos. Solitons & Fractals 45:539–547

56. Mirjalili S, Lewis A (2014) Adaptive gbest-guided gravitational search algorithm. Neural Comput Applic 25:1569–1584

57. Khajehzadeh M, Taha MR, El-Shafie A, Eslami M (2012) A modified gravitational search algorithm for slope stability analysis. Eng Appl Artif Intell 25:1589–1597

58. Han X, Chang X (2012) A chaotic digital secure communication based on a modified gravitational search algorithm filter. Inf Sci 208:14–27

59. Li C, Li H, Kou P (2014) Piecewise function based gravitational search algorithm and its application on parameter identification of avr system. Neurocomputing 124:139–148

60. Li P, Duan H (2012) Path planning of unmanned aerial vehicle based on improved gravitational search algorithm. Sci China Technol Sci 55:2712–2719

61. Davarynejad M, Forghany Z, van den Berg J (2012) Mass-dispersed gravitational search algorithm for gene regulatory network model parameter identification. In: Proc. of springer asia-pacific conference on simulated evolution and learning, Vietnam, pp 62–72

62. Mittal H, Pal R, Kulhari A, Saraswat M (2016) Chaotic kbest gravitational search algorithm (ckgsa). In: Proc. of IEEE international conference on contemporary computing, India

63. Feng Y, Teng G-F, Wang A-X, Yao Y-M (2007) Chaotic inertia weight in particle swarm optimization. In: Proc. of IEEE international conference on innovative computing, information and control, Japan, pp 475–480

64. Mittal H, Saraswat M (2018) An image segmentation method using logarithmic kbest gravitation al search algorithm based superpixel clustering. Evolutionary Intelligence: 1–13

65. Mittal H, Saraswat M (2018) An optimum multi-level image thresholding segmentation using non-local means 2d histogram and exponential kbest gravitational search algorithm. Eng Appl Artif Intell 71:226–235

66. Sridar P, Kumar A, Quinton A, Nanan R, Kim J, Krishnakumar R (2019) Decision fusion-based fetal ultrasound image plane classification using convolutional neural networks. Ultrasound in Medicine & Biology 45(5):1259–1273

67. Liu Z, Cao Y, Li Y, Xiao X, Qiu Q, Yang M, Zhao Y, Cui L (2020) Automatic diagnosis of fungal keratitis using data augmentation and image fusion with deep convolutional neural network. Computer Methods and Programs in Biomedicine 187:105019

68. Alom MZ, Taha TM, Yakopcic C, Westberg S, Sidike P, Nasrin MS, Van Esesn BC, Awwal AAS, Asari VK (2018) The history began from alexnet: a comprehensive survey on deep learning approaches. arXiv:1803.01164

69. Liu W, Wang Z, Liu X, Zeng N, Liu Y, Alsaadi FE (2017) A survey of deep neural network architectures and their applications. Neurocomputing 234:11–26

70. torchvision.models ? pytorch 1.5.0 documentation. https://pytorch.org/docs/stable/torchvision/models.html. Accessed on 31 May 2020

71. Pal R, Saraswat M (2018) Enhanced bag of features using alexnet and improved biogeography-based optimization for histopathological image analysis. In: 2018 eleventh international conference on contemporary computing (IC3). IEEE, pp 1–6

72. Pandey AC, Rajpoot DS (2020) Improving sentiment analysis using hybrid deep learning model. Recent Advances in Computer Science and Communications 13:1–20

73. Rashedi E, Nezamabadi-Pour H, Saryazdi S (2009) Gsa: a gravitational search algorithm. Inf Sci 179:2232–2248

74. Tsai H-C, Tyan Y-Y, Wu Y-W, Lin Y-H (2013) Gravitational particle swarm. Appl Math Comput 219:9106–9117

75. Wang M, Wan Y, Ye Z, Gao X, Lai X (2018) A band selection method for airborne hyperspectral image based on chaotic binary coded gravitational search algorithm. Neurocomputing 273:57–67

76. Sabri NM, Puteh M, Mahmood MR (2013) A review of gravitational search algorithm. International Journal of Advances in Soft Computing and its Application 5:1–39

77. Mittal H, Saraswat M (2019) An automatic nuclei segmentation method using intelligent gravitational search algorithm based superpixel clustering. Swarm and Evolutionary Computation 45:15–32

78. Brest J, Bošković B, Zamuda A, Fister I, Mezura-Montes E (2013) Real parameter single objective optimization using self-adaptive differential evolution algorithm with more strategies. In: Proc. of IEEE congress on evolutionary computation, Mexico, pp 377–383

79. Liu H, Wang Y, Tu L, Ding G, Hu Y (2018) A modified particle swarm optimization for large-scale numerical optimizations and engineering design problems. J Intell Manuf 29:1–27

80. Nagaraju S, Reddy AS, Vaisakh K (2019) Shuffled differential evolution-based combined heat and power economic dispatch. In: Proc. of Springer international conference on soft computing in data analytics, Singapore, pp 525–532

81. Pal R, Saraswat M (2019) Histopathological image classification using enhanced bag-of-feature with spiral biogeography-based optimization. Applied Intelligence 49(9): 3406–3424

82. Pandey AC, Rajpoot DS (2019) Spam review detection using spiral cuckoo search clustering method. Evol Intel 12:147–164

83. Pereira DG, Afonso A, Medeiros FM (2015) Overview of friedman's test and post-hoc analysis. Communications in Statistics-Simulation and Computation 44:2636–2653

84. ieee8023/covid-chestxray-dataset: we are building an open database of covid-19 cases with chest x-ray or ct images. https://github.com/ieee8023/covid-chestxray-dataset. Accessed 01 June 2020

85. Chest x-ray images (pneumonia) — kaggle. https://www.kaggle.com/paultimothymooney/chest-xray-pneumonia. Accessed 01 June 2020

86. Zhao J, Zhang Y, He X, Xie P (2020) Covid-ct-dataset: a ct scan dataset about covid-19. arXiv:2003.13865

87. jannisborn/covid19_pocus_ultrasound: open source ultrasound (pocus) data collection initiative for covid-19., https://github.com/jannisborn/covid19_pocus_ultrasound. Accessed 01 June 2020

88. Pal R, Saraswat M (2020) A new weighted two-dimensional vector quantisation encoding method in bag-of-features for histopathological image classification. International Journal of Intelligent Information and Database Systems 13(2-4):150–171